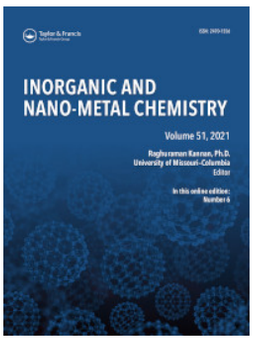

Inorganic and Nano-Metal Chemistry

ISSN: (Print) (Online) Journal homepage: https://www.tandfonline.com/loi/lsrt21

Metal borate nanostructures for industrial antibacterial ceramic fabrication

Osman Aguş, Osman Arslan & Yüksel Abalı

To cite this article: Osman Aguş, Osman Arslan & Yüksel Abalı (2021) Metal borate nanostructures for industrial antibacterial ceramic fabrication, Inorganic and Nano-Metal Chemistry, 51:6, 839-855, DOI: 10.1080/24701556.2020.1811328

To link to this article: https://doi.org/10.1080/24701556.2020.1811328

INORGANIC AND NANO-METAL CHEMISTRY
2021, VOL. 51, NO. 6, 839–855
https://doi.org/10.1080/24701556.2020.1811328

Metal borate nanostructures for industrial antibacterial ceramic fabrication

Osman Aguş[a], Osman Arslan[b], and Yüksel Abalı[a]

[a]Faculty of Science and Letters, Departmant of Chemistry, Manisa Celal Bayar University, Manisa, Turkey; [b]Faculty of Engineering and Natural Sciences, Departmant of Food Engineering, Istanbul Sabahattin Zaim University, Istanbul, Turkey

ABSTRACT

Silver and copper borate nanostructures were mechanistically synthesized for novel boron-containing antibacterial applications. Different concentration, temperature, time parameters were varied for obtaining hierarchical formulations. Metal borate nanostructures showed interesting crystalline and optical properties since temperature and concentration adjustments provided correlated shape and surface properties with around 300 nm size. Chemical analysis and crystallinity of both copper and silver formulations were conducted with X-ray diffraction and unveiled that especially temperatures ranging from 40 to 90 °C has a huge impact on the formation of nanostructures. X-ray photoelectron spectroscopy analysis comprehensively provided all atomic compositions especially about boron atom at 191–192 eV range. Additionally, energy-dispersive X-ray analysis with scanning electron microscope measurements revealed the morphological properties of the nanostructures and showed the purity of the obtained materials. Finally, metal borate-containing glazes were obtained on 1 × 1 cm samples for antibacterial tests against Gram-positive and Gram-negative microorganisms.

ARTICLE HISTORY
Received 17 June 2020
Accepted 26 July 2020

KEYWORDS
Antibacterial compound; silver borate; copper borate; nanoparticles; ceramic glaze; ceramic nanocomposite

Introduction

The microbial world is very active and old in the present world conditions.[1] Bacteria settle on different surfaces and spread through propagation.[2] In recent years, bacterial diseases have been reaching risky levels all over the world. Therefore, the studies of compounds that do not have a toxic effect on health and have both antibacterial and antioxidant activities should increase rapidly.[3] Antibacterial materials have been widely used in many products such as pigment,[4,5] water sterilization,[6,7] food packaging,[8,9] biomedicine,[10,11] and ceramics.[12] The nanoparticles (NPs) are intensively used for the administration of theranostics and the cure of infectious human diseases[13] in medical applications, drug delivery systems, bioactive compounds,[9] and coating.[14,15] There are many NP synthesis methods like bottom-up or top-down routes. Generally, bottom-up methods start with molecular precursors, whereas top-down methods follow the miniaturization of the amorphous structures.

NPs have high surface areas/volume ratios, which ensure that the particles have different chemical and physical properties than bulk materials.[16–19] In this context, the production of silver, copper, zinc oxide, and titanium dioxide NPs is intensively available in the production of antibacterial nanomaterials.[20–26] Additionally, these particles are also active in antivirus applications. Due to the current Covid-19 problem, possibly, antibacterial surfaces will also be antivirus types of materials and this phenomenon should be investigated.

Development and usage of antibacterial materials seem to be a very important subject in the human life. Various metal and metal oxide NPs are known and applied due to their huge activity for antibacterial properties, such as silver (Ag), copper (Cu), zinc (Zn), titanium (Ti), silicon (Si), magnesium (Mg), aluminum (Al), and their oxides.[9,27,28] Metal NPs, especially silver NPs have wide usage in new technologies such as electronics, materials science, and nanomedicine.[29,30] Silver NPs are used as antibacterial and antiviral materials in household appliances and aerogels,[31,32] whereas copper NPs are used in antibacterial applications.[33,34] Among other techniques, the preparation of hybrid surface coating is one of the most intensively highlighted methods in the fabrication of antibacterial surfaces.[20,35–40] The antibacterial effect is generally explained in three different mechanisms; ion release from the antibacterial agent or surface, light absorption, and active photocatalytic or other methods for the cell wall destruction or again cell wall destruction by some chemicals such as quaternary ammonium salts (Figure 1). Antibacterial properties of silver and its compounds were established for centuries[41,42] as silver ions, dissolved, and agitated from a silver-coated surface, can kill both Gr(+) and Gr(-) bacteria.[43] That's why, silver-containing products were used in various applications, including wound improvement,[44] eye infections,[45,46] urinary tract infections related to catheter-associated,[47,48] and ceramic surface.[12] In addition, the use of copper as an antibacterial

CONTACT Yüksel Abalı yuksel.abali@cbu.edu.tr Faculty of Science and Letters, Departmant of Chemistry, Manisa Celal Bayar University, Manisa 45140, Turkey.

Supplemental data for this article can be accessed at the publisher's website.

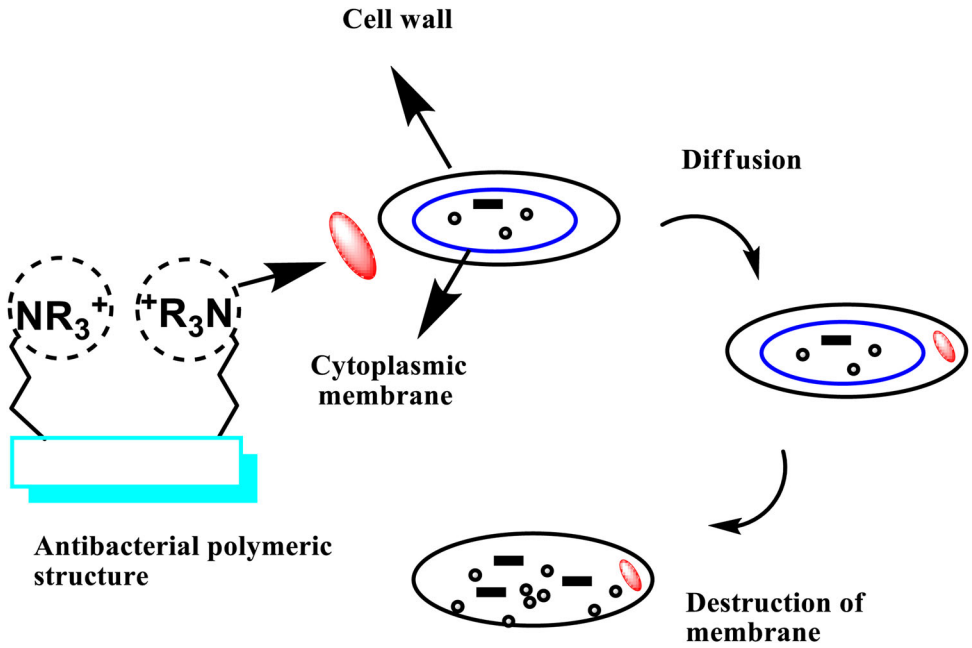

Figure 1. Antibacterial mechanisms with different active methods.

material won importance in the nineteenth and twentieth centuries and continued until antibiotic usage.[49] The use of copper in copper containers or glass bottles containing copper coils has recently been reported by Sudha et al.,[50] it was proposed by as a domestic water purification method to remove enteric bacteria and make water drinkable, especially in developing countries.

Nanocomposite structures have more than one component and can be used in many different applications. NPs introduced nanocomposite systems generally depend on the silicon-based precursors together with epoxy, acrylic, or polyurethane polymers. Therefore, antibacterial applications with common metal structures are wide for nanocomposites.[51–54]

As generally known metal borate nanostructures consist of boron, oxygen, metal, and hydrogen where boron atoms are connected to oxygen aroms for their low coordination. There may also be water and hydroxyl groups in the crystal structure. Trihedral and tetrahedral boron oxygen structures are the basic structures of metal borates.[55,56] Copper borate compounds include borates like CuB_2O_4, $CuBO_2$, $Cu_3B_2O_6$, $Cu_2[BO(OH)_2](OH)_3$, $Cu_3B_6O_{12}H_20$, and $Cu_3B_6O_{12}$.[57] Fine-grained, blue, and long-standing aqueous copper borates, such as $2CuO{\cdot}B_2O_3{\cdot}3H_2O$ and $3CuO{\cdot}2B_2O_3\ nH_2O$ ($n = 5, 4, 2, 1$), have also been synthesized.[58] In addition, some synthetic borates are also described. These borates listed as: $Na_6\{Cu_2[B_{16}O_{24}(OH)_{10}]\}\ 12H_20$,[59] $K_5H\{Cu_4O[B_{20}O_{32}(OH)_8]\}\ 32H_2O$,[60] and $Cu(NH_3)\ 4B_4O_76H_20$.[61]

In this detailed investigation, we have developed silver and copper borate nanostructures and conducted a detailed physical and chemical investigation for crystallinity, optical properties, and surface features together with their antibacterial activities on ceramic surfaces. Results revealed that these borate nanostructures are the potential candidates for an industrial antibacterial application.

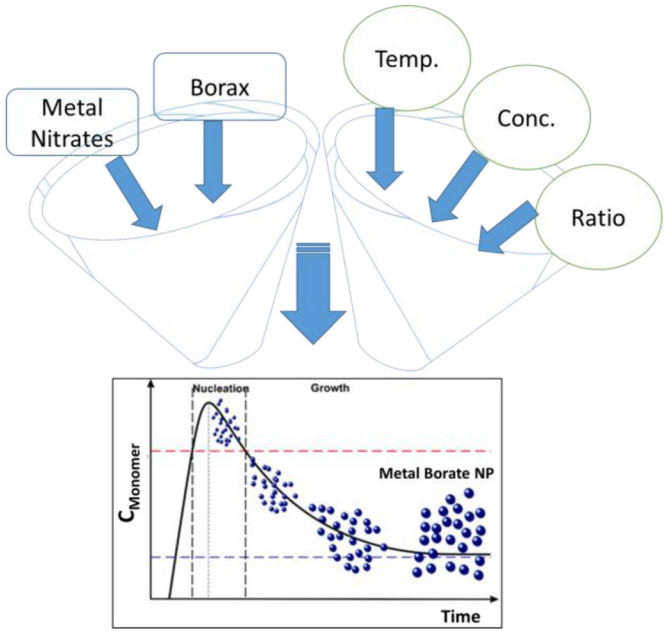

Figure 2. Scheme for the reaction components and particle formation.

Materials and methods

Materials

For the synthesis, borax used as beginning material (disodium tetraborate decahydrate ($Na_2B_4O_7{\cdot}10\,H_2O$) (Merck), silver nitrate ($AgNO_3$) (Nalgene), and copper (II) nitrate trihydrate ($Cu(NO_3)_2{\cdot}3H_2O$) (Merck) were reacted for the mechanistic synthesis of silver borate and copper borate NPs. All the materials were used as purchased. Solutions were prepared before mixing and all the reactions were repeated as completely identical by changing the necessary parameters. At the end of the reactions, obtained samples were filtered, separated, and dried.

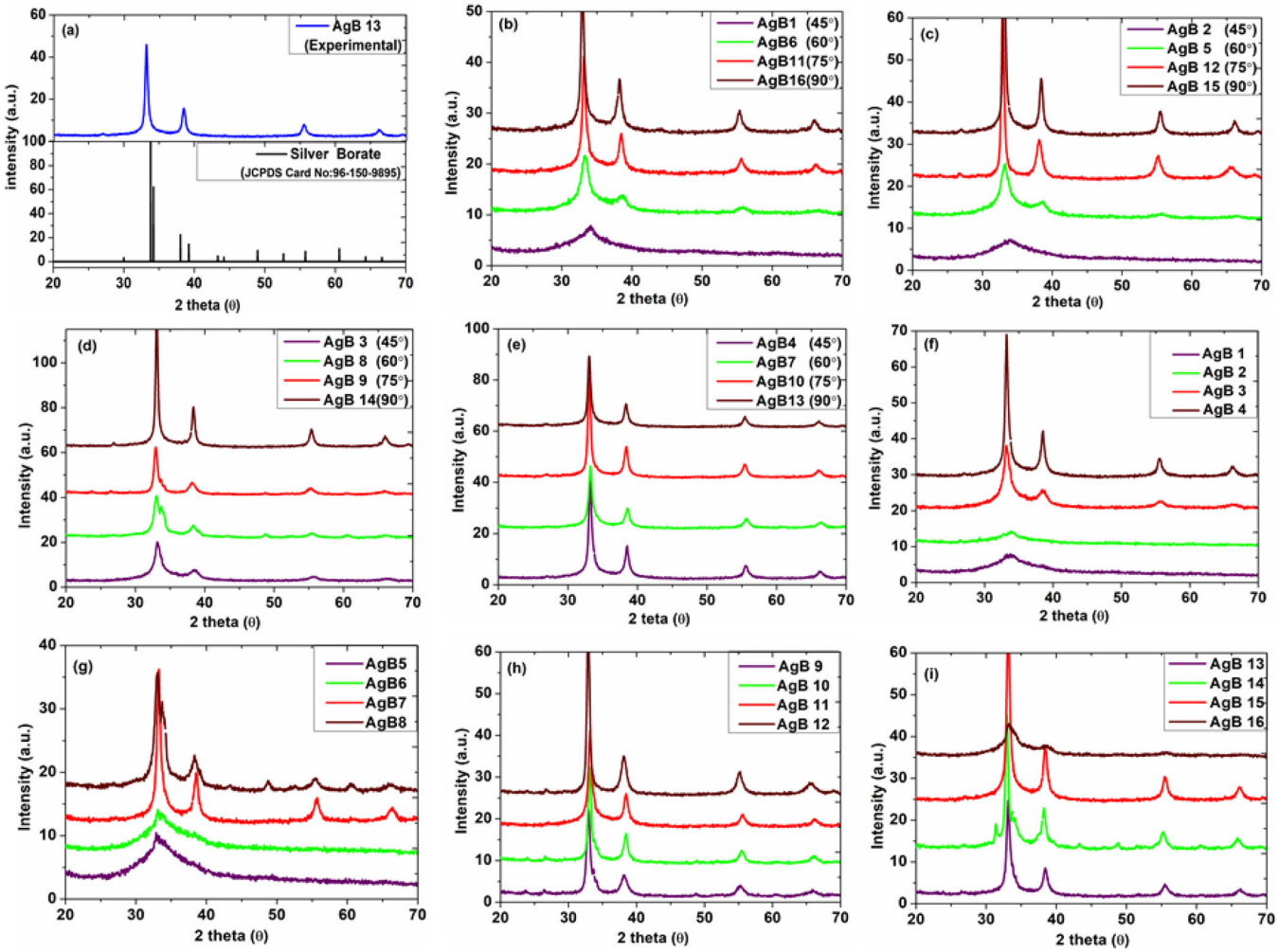

Figure 3. XRD results of the silver borate experiments. (a) Comparison of the synthesized AgB13 with JCPDS: 96-150-9895 peaks, (b) silver borate formation mole ratios silver/borax at 1/2, (c) mole ratios silver/borax at 1/1.5, (d) mole ratios silver/borax at 1/1, (e) mole ratios silver/borax at 2/1, (f) silver borate formation at 45 °C, (g) at 60 °C, (h) at 75 °C, (i) at 90 °C.

Methods

The X-ray diffraction (XRD) (Philips X'Pert Pro) patterns have been obtained by using Cu Ka radiation in a range of $2\theta = 20–80$ by using enough amount of solid particles. The elemental composition investigation (energy-dispersive X-ray analysis [EDX]) of the obtained structures was performed together with morphology and the size analyses with a scanning electron microscope (SEM) (Philips XL 30S FEG). In order to avoid the electron charging effect, samples were coated with 5 nm Au (Leica) prior to the SEM imaging. Dispersed particles were dropped on a carbon tape and dried. Average sizes were calculated by counting and measuring 50–100 particle diameters and plotting them with respect to their frequencies. Non-linear fitting on the obtained particles gave an average value with a calculated statistical standard deviation. The surface and elemental composition of the dried NPs were performed by X-ray photoelectron spectroscopy (XPS, Thermo Scientific, Kα). XPS spectra have been obtained by a flood gun charge neutralizer system equipped with a monochromated Al Kα X-ray source ($h\nu = 1486.6$ eV) from 400 mm spot size on the NPs. Wide energy survey scans have been recorded between 0 and 1360 eV binding energy range, at detector pass energy of 200 eV, and with energy step size of 1 eV. High-resolution spectra were obtained at pass energy of 50 eV and with energy steps of 0.1 eV for each atom. FT-IR spectra were recorded by dried NPs in between 400 and 4000 cm^{-m} with Agilent 600 series ATR module spectrophotometer. UV-Vis absorption properties of the NPs in EtOH dispersion were conducted by UV-Vis spectrophotometer in between 200 and 800 nm (Agilent Cary 60 UV-Vis Spectrophotometer). Thermal properties of the obtained particles were measured between room temperature and 1000 °C with 20 °C/min increasing rate under N_2 atmosphere by the TGA Shimadzu DTG-60 series. Generally, the amount of the particles was below 10 mg.

Antibacterial tests of silver borate and copper borate NPs were obtained with *Staphylococcus aureus* (ATCC 6538 Gram-positive) and *Escherichia coli* (ATCC 25922 Gram-negative) bacteria. Activation of the ATCC cultures was realized with −80 °C storage and cultures were formed by planting Petri plates with nutrient agar (Merck) and Mueller Hinton broth (MHB) (Merck). Nutrient broth (NB) and dilution method were utilized to observe the antibacterial

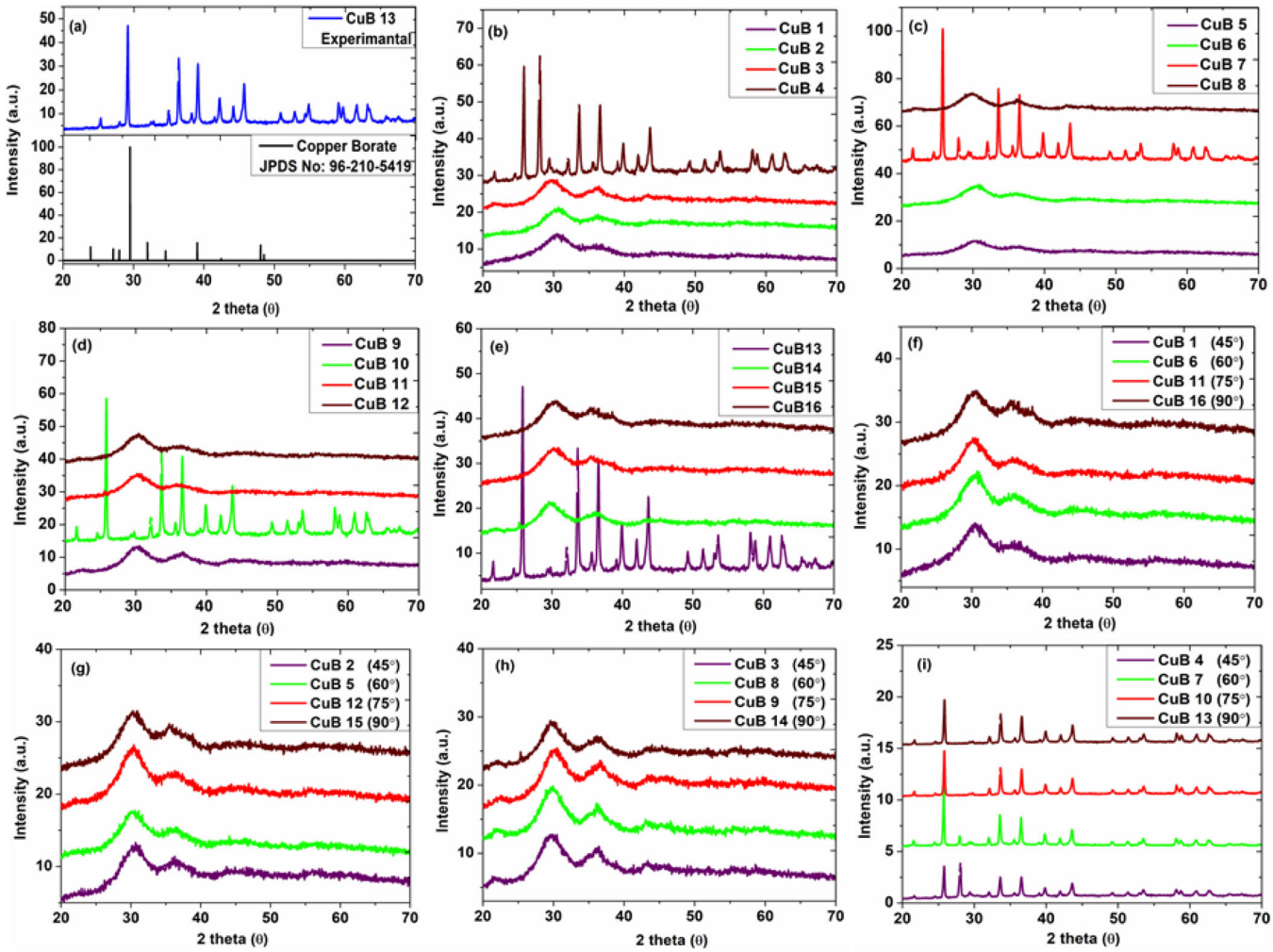

Figure 4. (a) Peaks of main copper borate and its comparison with obtained sample (CuB13), (b) copper borate formation at 45 °C, (c) at 60 °C, (d) at 75 °C, (e) at 90 °C, (f) copper borate formation mole ratios copper/borax at 1/2, (g) mole ratios copper/borax at 1/1.5, (h) mole ratios copper/borax at 1/1, (i) mole ratios copper/borax at 2/1.

activity of the nanomaterial. Produced solutions with bacteria were set to 0.5 McFarland turbidity by sterile PBS, after 24 h of incubation at 37 °C.

Fabrication of silver and copper borate nanoparticles

Silver nitrate ($AgNO_3$) and borax ($Na_2B_4O_7.10\,H_2O$) were mixed with different proportions of $AgNO_3/Na_2B_4O_7{\cdot}10\,H_2O$ at four different temperatures such as 45, 60, 75, and 90 °C. Before the reactions, completely dissolved solution was prepared. Also, copper nitrate ($Cu(NO_3)_2{\cdot}3H_2O$) and borax ($Na_2B_4O_7{\cdot}10H_2O$) were treated together at four different temperatures with varying molar ratios of $Cu(NO_3)_2{\cdot}3H_2O/Na_2B_4O_7{\cdot}10\,H_2O$. Temperatures of the solutions were arranged in an oil bath. Also, the reaction time has been changed for all the experiments. All procedures may be found in Supplementary Table S1. Figure 2 represents the general method and formation dynamics for obtained silver borate and copper borate NPs.

During the reaction, as soon as borax was added to the silver or copper solution, a nucleation formation was observed immediately. Metal nitrate structures have +1 and +2 oxidation values. This means chemical interaction between the borate structure arising from borax and metal cations should react in certain proportions. Since oxidation value for zinc and copper is +2, borate structures can form ring-type structures where zinc and copper bind three borate structures. But for silver cation, it can basically replace the sodium atoms in the nanostructure. Therefore, copper borate is formed only if the metal cation is in very certain proportions for the rapidly growing structures. After the reaction, silver borate and copper borate NPs have been synthesized which investigated by XRD and SEM for other applications. Prior to the examination, NP samples were bathed and dry particles obtained with EtOH.

Results and discussion

Crystallinity of the silver and copper borate NPs

The structure and pureness of the mentioned phase of the synthesized silver borate and copper borate NPs were investigated with XRD. Characteristic XRD peaks of silver borate NP, which was compared with its original XRD data, hexagonal silver borate form with JCPDS card no: 96-150-9895 with formula Ag_3BO_3 was showed in Figure 3a. Enlarged

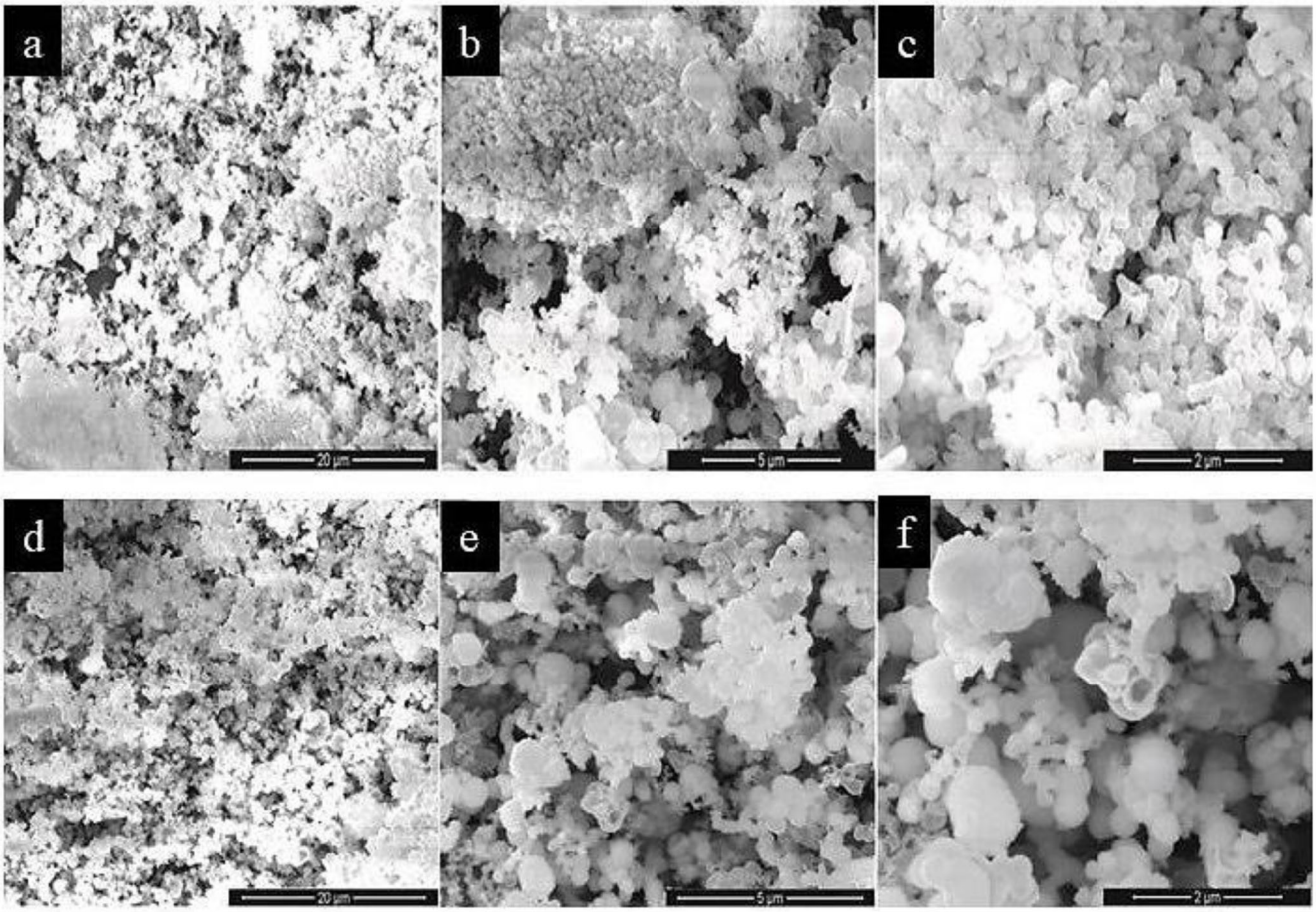

Figure 5. Representative SEM image of the silver borate (AgB13) at 90 °C, Ag/B_2O_3 mole ratio 2:1. (a) 20 µm, (b) 5 µm, (c) 2 µm (AgB16) at 90 °C, Ag/B_2O_3 mole ratio 1:2 (d) 20 µm, (e) 5 µm, (f) 2 µm magnification values.

XRD peaks of silver borate structures are monitored related to the real crystalline data with 2θ values of 30.00°, 33.20°, 33.79°, 34.19°, 38.04°, 39.21°, 43.33°, 44.21°, 48.99°, 52.66°, 55.77°, 60.56°, 64.31°, 66.61°, and 77.32°. For this reason, nucleation, which also affects particle formation, does not occur at the required rate. The peaks at 33.20°, 38.50°, 55.60°, and 66.10° are distinguishable for AgB_4 and AgB_3 enterprises.

Surprisingly, XRD peaks unveiled that by enhancing the temperature, the peak density of the synthesized particles increased. It is likely excessive anions of borate ions are governing the solution dynamics by changing the hydrogen concentration, flux rate, and appropriate complex formation. The most salient note which can be derived from the reactions is that the formation and crystallinity of silver borate occur at increasing temperatures and role of the mole ratio seems ineffective in the same regions. The intensity of XRD patterns was expressively increased with the increasing temperature. The effect of temperature speeds up formation of the particle conditions such as formation of extremely crystalline structures, increased atomic diffusion, increased saturation, and sufficient flux ratio in solution (Figure 3b–e). In Figure 3b–e, all the peaks were analyzed according to the varying mole ratios. This means, silver and borax ratios were kept stable with four different applications. In Figure 3b, Ag/borax ratio was 1/2 and it is easily seen that increasing temperature forms a very high crystallinity. Figure 3c,d show that if the ratio was changed to 1/1.5 and 1/1, formation of the silver borate at low temperatures is very sensitive and especially 1/1.5 has a very low crystallinity. Still when the silver ratio increases to 2 versus borax 1, as in Figure 3e, quite perfect crystal structures are observed. If one compares all the 16 XRD investigations here, it is obvious that temperature regulates the real silver borate crystal formation and mole ratio is actually not effective as much as the temperature.

Therefore, in Figure 3f–i, the analysis of the XRD results was redesigned according to the temperature parameter. In Figure 3f,g, low-temperature peaks like 45 and 60 °C were graphically presented. It is clearly seen that the formation of the silver borate crystals is hardly realized, but in the proportions of 2/1 (silver/borax), crystallinity is still high. But when we focus on the high temperatures namely 75 °C and 90 °C, it is possible to see silver borate crystals at any mole ratio (Figure 3h,i). Hence, we can conclude that temperature acts an important role in the formation of the silver borate nanocrystals. Also, this mechanistic study can reveal the small details concerning the XRD peaks of the silver borate crystals. For example, the noise-to-peak ratio is highly acceptable in high temperatures and high silver molar ratios. This can also be seen and compared in low-temperature XRD peaks.

When XRD peaks of copper borate are examined with characteristic XRD peaks of copper borate NPs, rectangular copper borate form with JCPDS: 96-210-5419 with formula

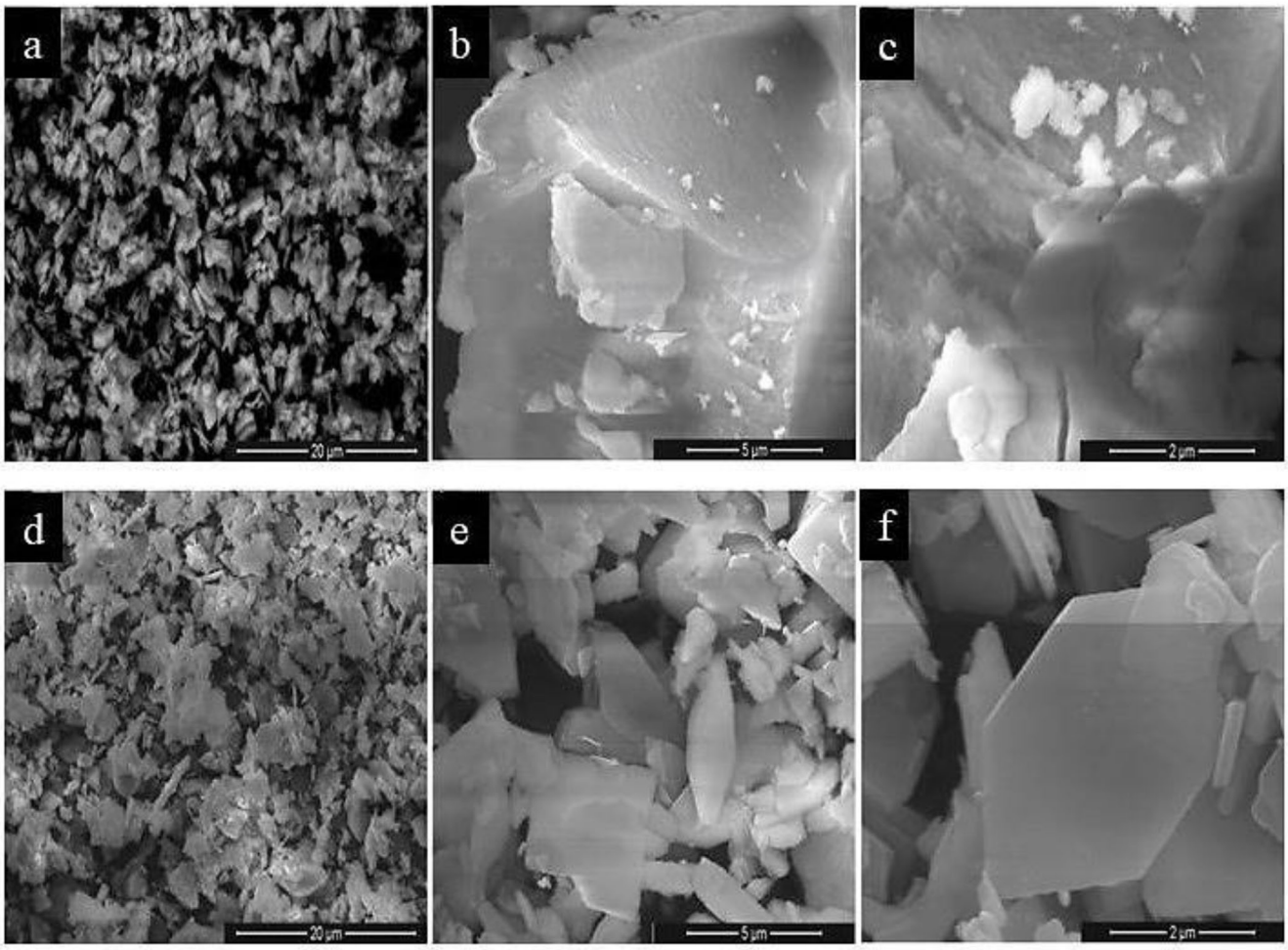

Figure 6. Representative SEM image of the copper borate (CuB13) at 90 °C, Cu/B_2O_3 mole ratio 2:1. (a) 20 µm, (b) 5 µm, (c) 2 µm (CuB16) at 90 °C, Cu/B_2O_3 mole ratio 1:2 (d) 20 µm, (e) 5 µm, (f) 2 µm magnification values.

$Cu_2(BO_3)_2$ patterns can be followed. A value of Bragg reflections with 2θ values of 23.90°, 29.51°, 34.50°, 39.06°, 42.4°, and 48.04° are observed (Figure 4a).

It is seen that the highest intensity of the copper borate formation occurs when the Cu/borax mole ratio is 2/1. According to the XRD results, increasing the molar ratio of copper concentration has shown that it reduces the peak density of the synthesized particles (Figure 4b). It can be stated that the formation of copper borate doesn't occur unless the molar ratios are proper like 2/1 Cu/borax.

Therefore, at almost any temperature, formation is related to the presence of Cu/borax ratio and independent from the temperature (Figure 4b–e). This result can also be supported when all the graphics were redesigned according to the molar ratios (Figure 4b–e) and different temperatures (Figure 4f–h). In Figure 4i, the molar ratio for Cu/borax is 2/1 which is perfectly ideal for the copper borate particle formation.

Still one can observe that at low temperatures like 45 °C intensity of the peaks are relatively smaller when compared to other temperatures. However, peak positions are clear and there is no discussion about the position of the peaks. Consequently, we can conclude that in silver borate NPs, temperature plays a huge role but when we switch to the copper borate, molar ratios are much more important factor than the temperature.

Morphology and composition

From the XRD characterization, we have concluded that some particles are more suitable for further use and examination. Therefore, we have utilized two different silver borate and two different copper borate nanoparticles as sample investigation. Atomic analysis and morphology investigation of the obtained NPs were realized by SEM and EDX. Monitored structures were prepared with alcohol (EtOH), then ultrasonication was performed. After that, a drop of this alcoholic solution was placed on carbon tape. To improve image quality, 5 nm Au (gold) was coated.

In the examination, it was seen that AgB13 (Figure 5a–c) and AgB16 (Figure 5d–f) NPs are spherical, CuB13 (Figure 6a–c) and CuB16 (Figure 6d–f) are plate-shaped, and there are no other impurities in the products. For AgB13 spherical particles, it was observed that inner sides of the spheres are empty and particle distribution is presenting a narrow range. Additionally, the porosity of the particles is high. When compared, the porosity of the AgB16 seems higher than AgB13 possibly due to the different particle sizes. Especially, AgB16 structure seems more complex since some of the particles show irregularities and distribution reflects a wider size band. Some particles are relatively large but less in

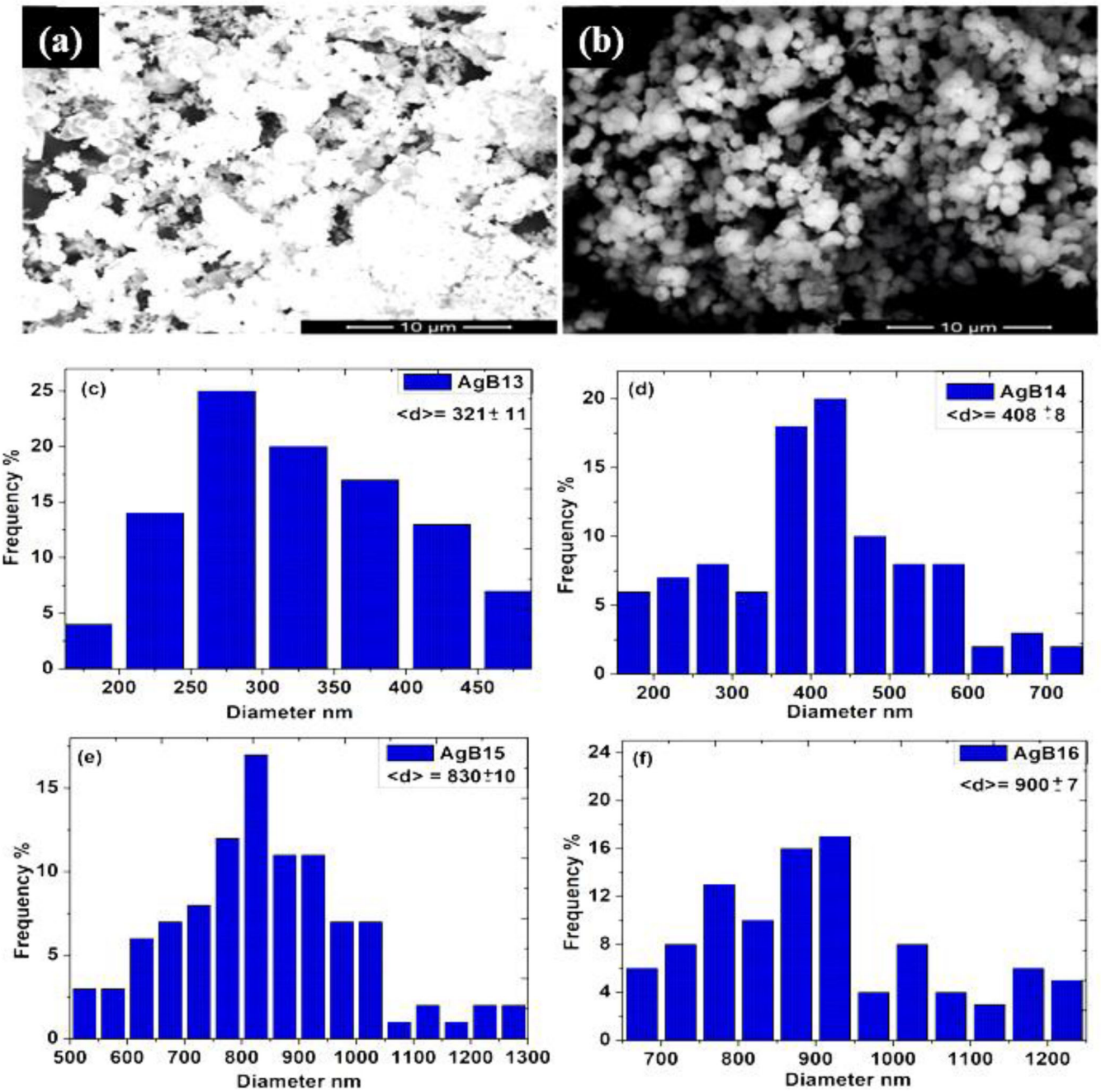

Figure 7. Representative SEM image of the silver borate for other 90 °C particles of (a) AgB14 (Ag/B_2O_3 mole ratio 1:1) (10 µm) and (b) AgB15 (Ag/B_2O_3 mole ratio 1:1.5) (10 µm), particle size distribution of the (c) AgB13, (d) AgB14, (e) AgB15, and (f) AgB16 samples.

number. With increasing scale, larger particles get more noticeable. From the measurements of SEM images (Figure 7a,b), the particle size of the synthesized AgB13 nanostructures (Figure7c–f) was determined as 321 nm on average (Figure 7c), whereas the AgB16 particles were larger and an average of 900 nm (Figure 7f).

The morphology and particle sizes of CuB13 particles (Figure 8a–d) were determined to be 754 nm on average (Figure 8c). Due to the irregular and layered structure of CuB16 particles, the dimensions of the particles can be imagined as two-dimensional and the layer thicknesses were measured between 150 and 200 nm (Figure 8d). Porosity of the CuB13 particles is higher than CuB16 since CuB16 has plate-like structure.

As stated before, silver and copper borate structures show different morphologies. When we compared the crystallinity and morphology, it is easier to detect the sample NP which can be used for further applications. From this viewpoint, other SEM images for silver borates with different mole proportions at 90 °C results were also investigated (Figure 7a,b). These samples are other 90 °C results for 1/1 and 1/1.5 mole ratios of the silver borate (Figure 7d,e).

Silver borate SEM investigation results clearly showed the similar morphology behavior for the 90 °C NPs formation. Interestingly, there is a linear increase in the average particle size distribution with the increasing Ag/borax amounts. This was also shown in Figure 9a. In lower proportions, the

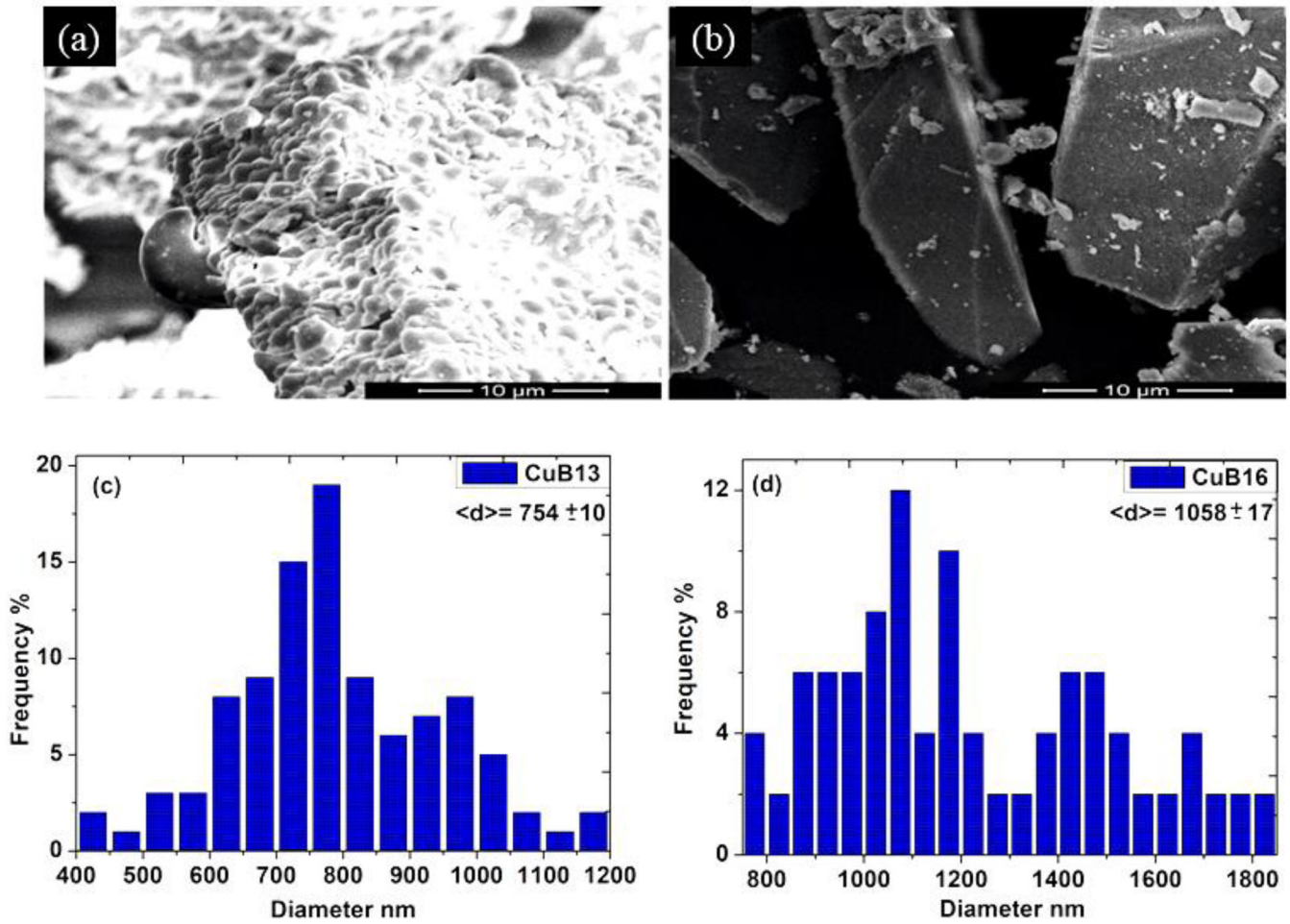

Figure 8. Representative SEM image of the copper borate 90 °C structures for (a) CuB14 (Cu/B_2O_3 mole ratio 1:1) (10 µm) and (b) CuB15 (Cu/B_2O_3 mole ratio 1:1) (10 µm), particle size distribution of the (c) CuB13 (Cu/B_2O_3 mole ratio 2:1) and (d) CuB16 (Cu/B_2O_3 mole ratio 1:2) samples.

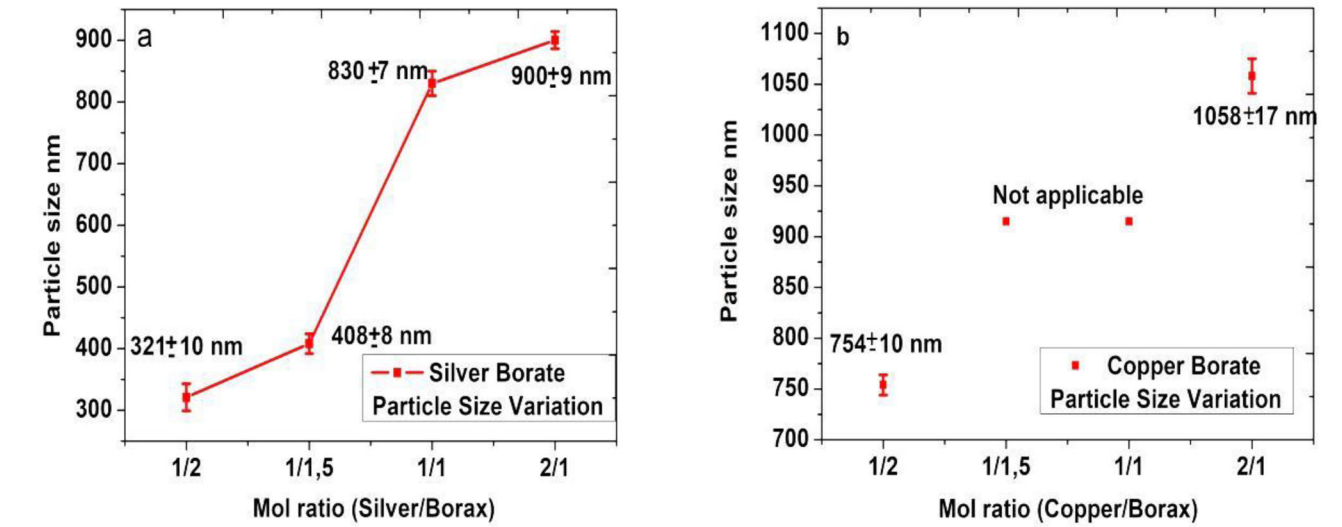

Figure 9. Particle size variation of the (a) AgB and (b) CuB samples.

particle size was detected as 321 nm, but when the proportion was increased to 2/1 average size was detected as 900 nm. Still, the size is under micrometer range and general morphology is similar in all proportions.

When we analyzed the particle sizes of the CuB samples obtained at 90 °C, we can also see a similar trend since it is clear that Cu/borax proportion defines the particle size (Figure 9b). As the borax amount increases the observed average particle sizes also increase as seen in Figure 8c,d even though a regular distribution couldn't obtain for CuB14 and CuB15. From the SEM images, in Figure 8a,b, it can be seen that the particle structure of the CuB14 and CuB15 samples

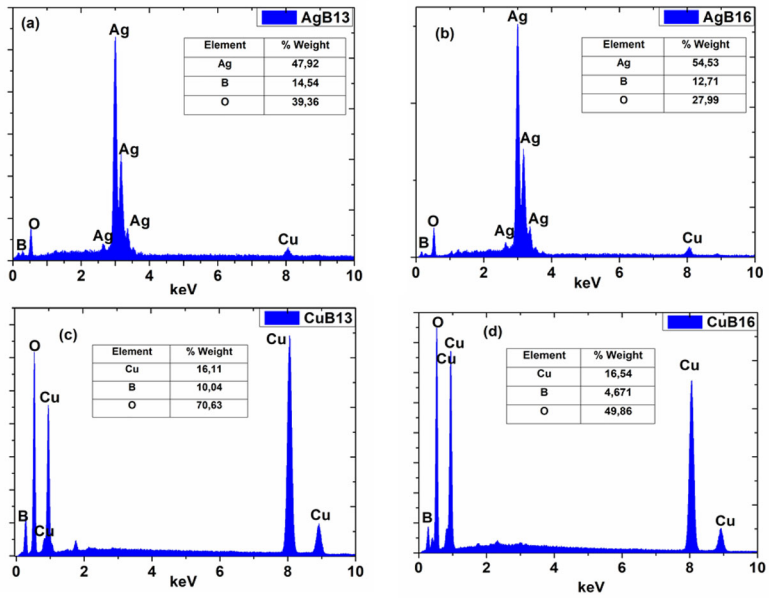

Figure 10. EDX curves of synthesized at 90 °C. (a) AgB13 (Ag/B_2O_3 mole ratio 2:1), (b) AgB16 (Ag/B_2O_3 mole ratio 1:2), (c) CuB13 (Cu/B_2O_3 mole ratio 2:1), (d) CuB16 (Cu/B_2O_3 mole ratio 1:2).

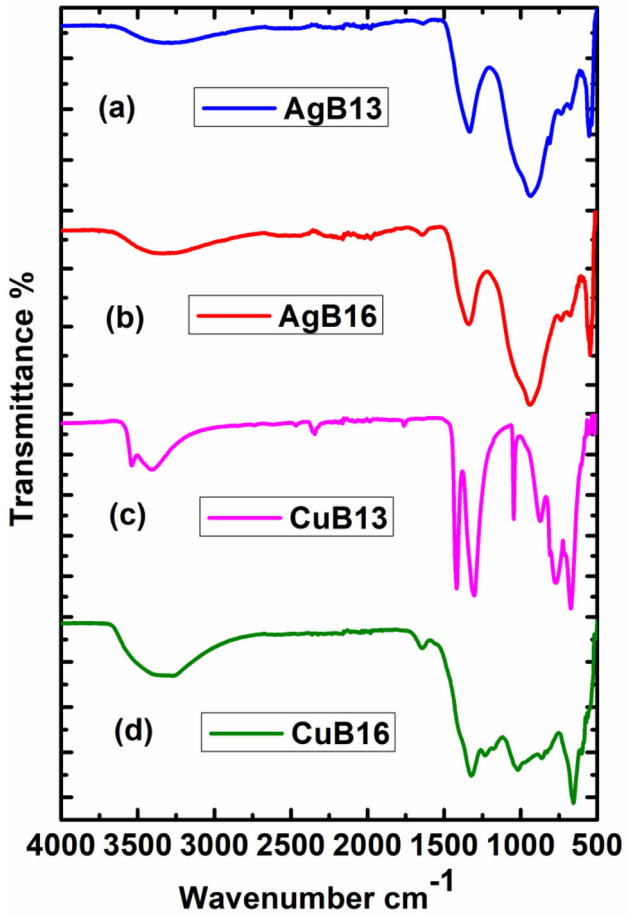

Figure 11. FT-IR curve of synthesized at 90°. (a) AgB13 (Ag/B_2O_3 mole ratio 2:1), (b) AgB16 (Ag/B_2O_3 mole ratio 1:2), (c) CuB13 (Cu/B_2O_3 mole ratio 2:1), and (d) CuB16 (Cu/B_2O_3 mole ratio 1:2).

are not having a regular shape – large and irregular. For this, the particle size of copper borate samples prepared at 1/1 and 1/1.5 mole ratios at 90 °C could not be measured.

Atomic analysis of chemical structure made by the EDX method, the existence of B, O, Ag, and Cu elements of silver borates and copper borates were determined (H was ignored) and presented in (Figure 10a–d). Masking agents or other types of atoms, for example, sodium was not observed. This investigation clearly shows the metal borate formation with high purity. Calculated atomic proportions were also showed as insert pictures on EDX graphs.

Surface characterization

Surface characteristics were characterized with FT-IR spectrometer on Agilent 600 series ATR module spectrophotometer. The wave number ranges from 4000 to 500 cm at a resolution of 4 cm^{-m}.

FT-IR analysis was performed to investigate the molecular bond characterization of the NP structure for AgB13 and AgB16. Observed characteristics were shown in Figure 11a–d. For FT-IR analysis, NPs were dried and measured immediately. For the borate structures, B-O symmetrical or asymmetrical tension peaks are visible at 890 cm^{-1} and 1350 cm^{-1} in both products, and they are connected with B-O bonds for the repeating B_4-O and B_3-O units, respectively. In-plane bending peaks for the same are detected at 511 cm^{-m} and 592 cm^{-m} which is related to the twisting of the B-O-B connections in the metal borate nanostructures.[62] Therefore, in addition, full surface analysis of the NP was conducted using the XPS method. Especially, the oxidation number of the metals was obtained.

The weak peak of 1600 cm^{-m} indicates the presence of water which is very general in similar compounds. Stretching band with H-bonding interaction of O-H is visible at 3400 cm^{-m}.[63] Similarly, FT-IR plots of the synthesized CuB13 and CuB16 structures were examined in Figure 11c,d. In these spectra, the band between 3250 and 3500 cm^{-m0} shows the O-H group, and H-O-H bond was observed at 1600 cm^{-m}. This band belongs to water molecule.

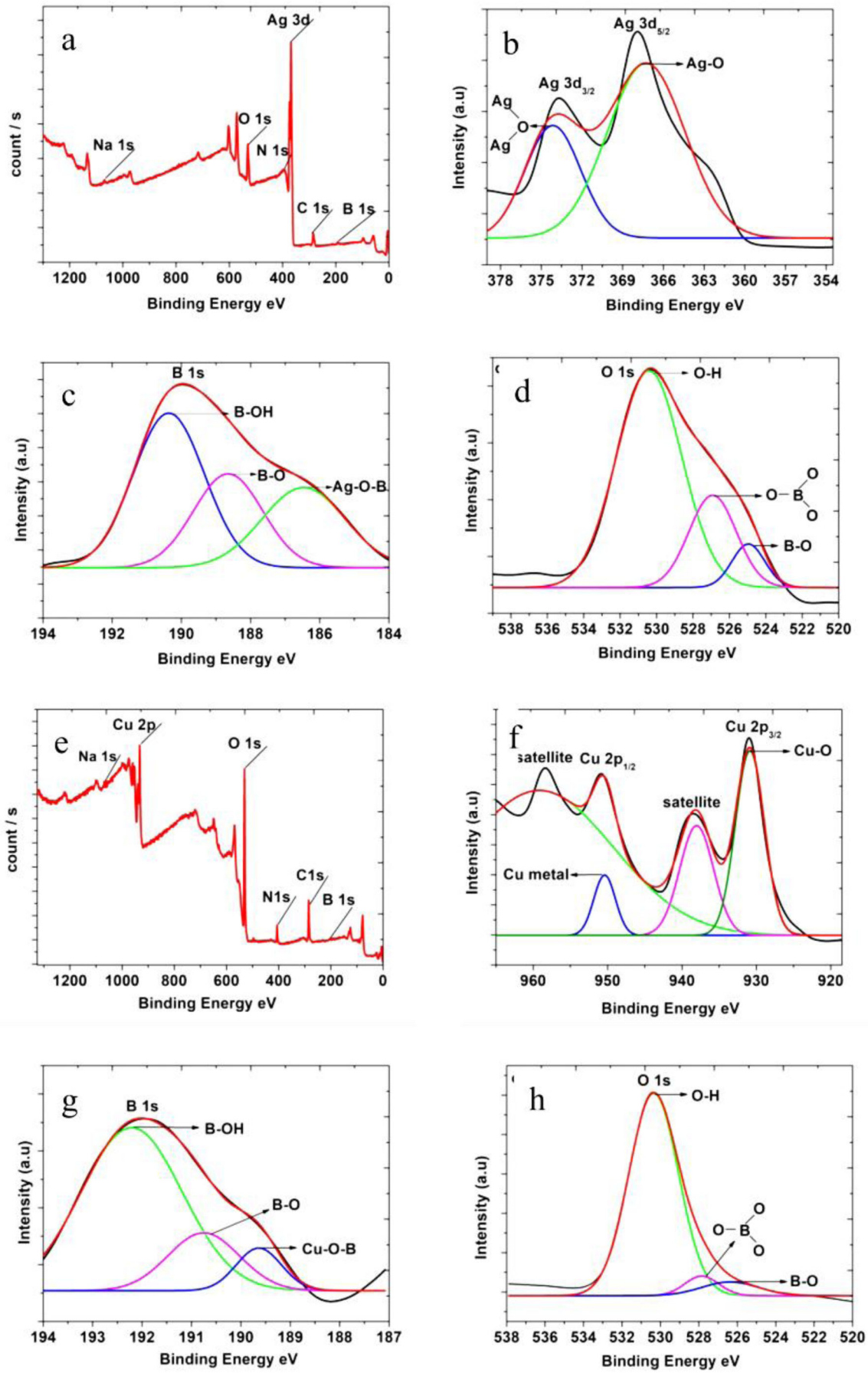

Figure 12. The XPS spectra at 90 °C with Ag(Cu)/B_2O_3 mole ratio 2:1. (a) AgB13 survey, (b) Ag3d core spectra, (c) B1s core spectra, (d) O1s core spectra of the sample AgB13, (e) CuB13 survey, (f) Cu2p core spectra, (g) B1s core spectra, (h) O1s core spectra of the sample CuB1.

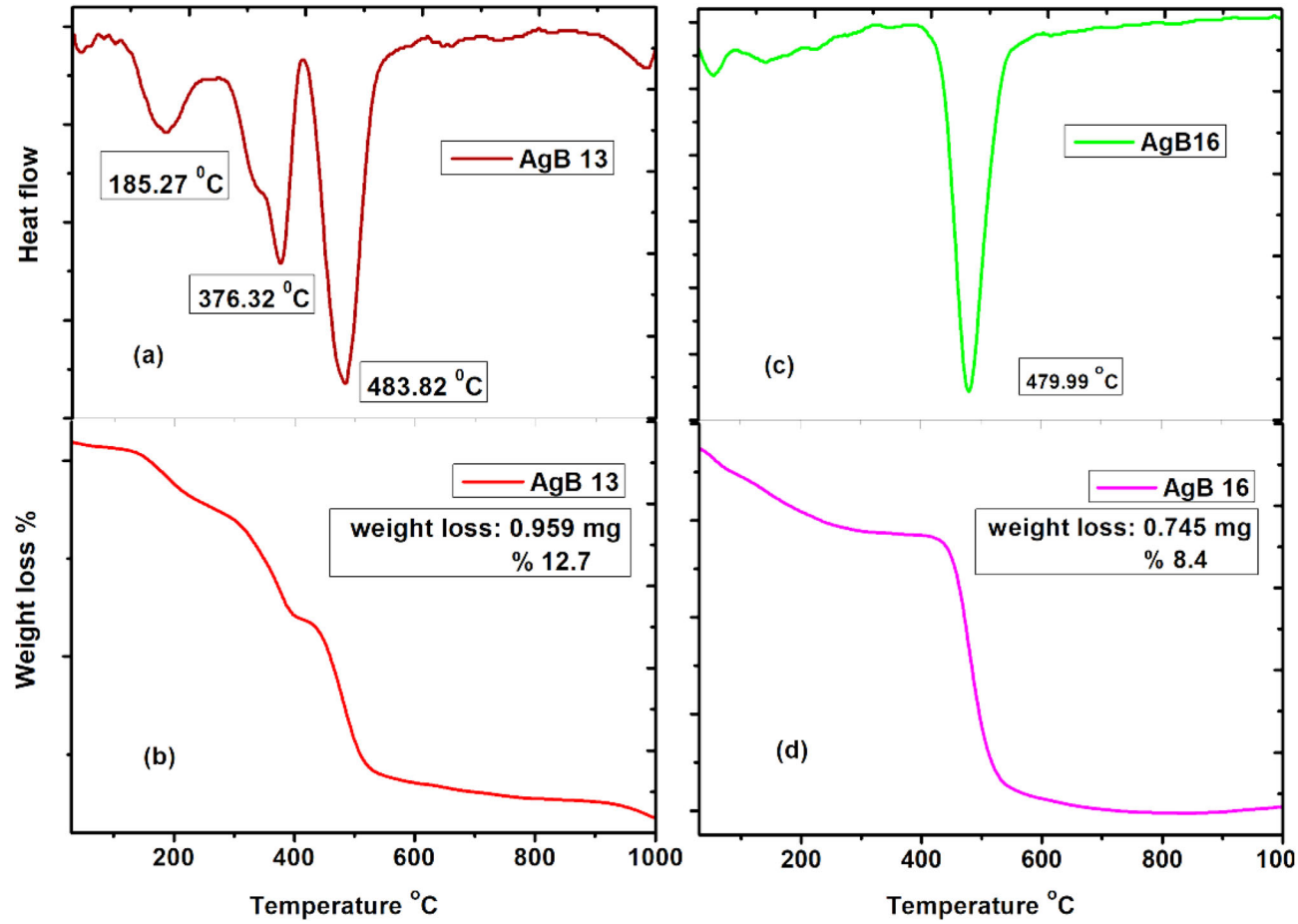

Figure 13. (a) DTA analysis of synthesized AgB13 at 90 °C (Ag/B_2O_3 mole ratio 2:1), (b) TGA graph of obtained AgB13, (c) DTA curve of synthesized AgB16 at 90 °C (Ag/B_2O_3 mole ratio 1:2), (d) TGA graph for AgB16.

Additionally, detected band in the fingerprint region, 1353–1252 cm^{-m} shows the band B-O stretching vibration, whereas the band between 1090 and 981 cm^{-m} shows the asymmetric B_4-O stretching. Other detectable peaks are at 941–865 cm^{-m} shows the B_3-O stretch and the peak at 782–730 cm^{-m} shows symmetrical B_3-O stretch.[64] FT-IR results clearly show that obtained particles are desired metal borate structures. Additionally, crystal water is detectable for these metal borate structures. It is possible to detect B-O Cu-O and Ag-O peaks but especially CuB16 sample shows small variations at 1500–1300 cm^{-m} which possibly arises due to the inefficient saturation of the Cu and borax reaction. Surface –OH groups are still visible and can be detected as shown in all spectra. Additional surface analysis and bonding properties were investigated using the XPS method.

X-ray photoelectron spectroscopy

The surface features and elemental mapping of metal borate nanostructures were completed by XPS. XPS spectra are gained by a flood gun charge neutralizer system which was connected to a monochromatic Al Kα X-ray source ($h\nu = 1486.6$ eV). Spot size was 400 mm and wide energy scans were recorded between 0 and 1360 eV binding energy range. Also, machine was conducted with detector pass energy of 200 eV and with energy step size of 1 eV. High-resolution XPS peaks were obtained with 50 eV transition energy and 0.1 eV energy steps for each atom.

Survey XPS also clearly indicates the presence of all atoms together with C and Na peaks (Figure 12a). Two peaks may be seen in Figure 12b – Ag 3d core-level XPS spectrum at 367.88 and 373.68 eV for Ag 3d5/2 and Ag 3d3/2, respectively.[65] Additionally, for the B atom 1s peak centers at 189 eV which can be appointed to B-OH and the other two peaks at 188 eV and 186 eV for the B-O and Ag-O-B, respectively.[66] The core spectra of B 1s for AgB13 shows peak at 186 eV indicating the presence of boron atom in the sample clearly (Figure 12c). The band in AgB13 can be attributed to replace the boron atom to oxygen atom in AgB13 lattice and mixing of B(2p) and O(2p) orbitals.[67] For the O 1s peaks in (Figure 12d), a major broad peak at 530.38 eV was due to hydroxyl, while the peak at 527 eV belongs to borate form. The binding energy at 530.38 eV for O 1s peak clearly shows the existence of B2O3 species, which is compatible with the B 1s peak at 189.98 eV of oxidized boron species.[68] As for the CuB13, survey XPS also clearly indicates the presence of all atoms together with C and Na peaks (Figure 12e). Cu 2p core level spectrum in Figure 12f represents two visible peaks positioned at 931.08 eV and 958.38 eV which correspond to Cu $2p_{3/2}$ and Cu $2p_{1/2}$, respectively. The Cu 2p peaks for the CuB13 samples look symmetrical but satellites are also

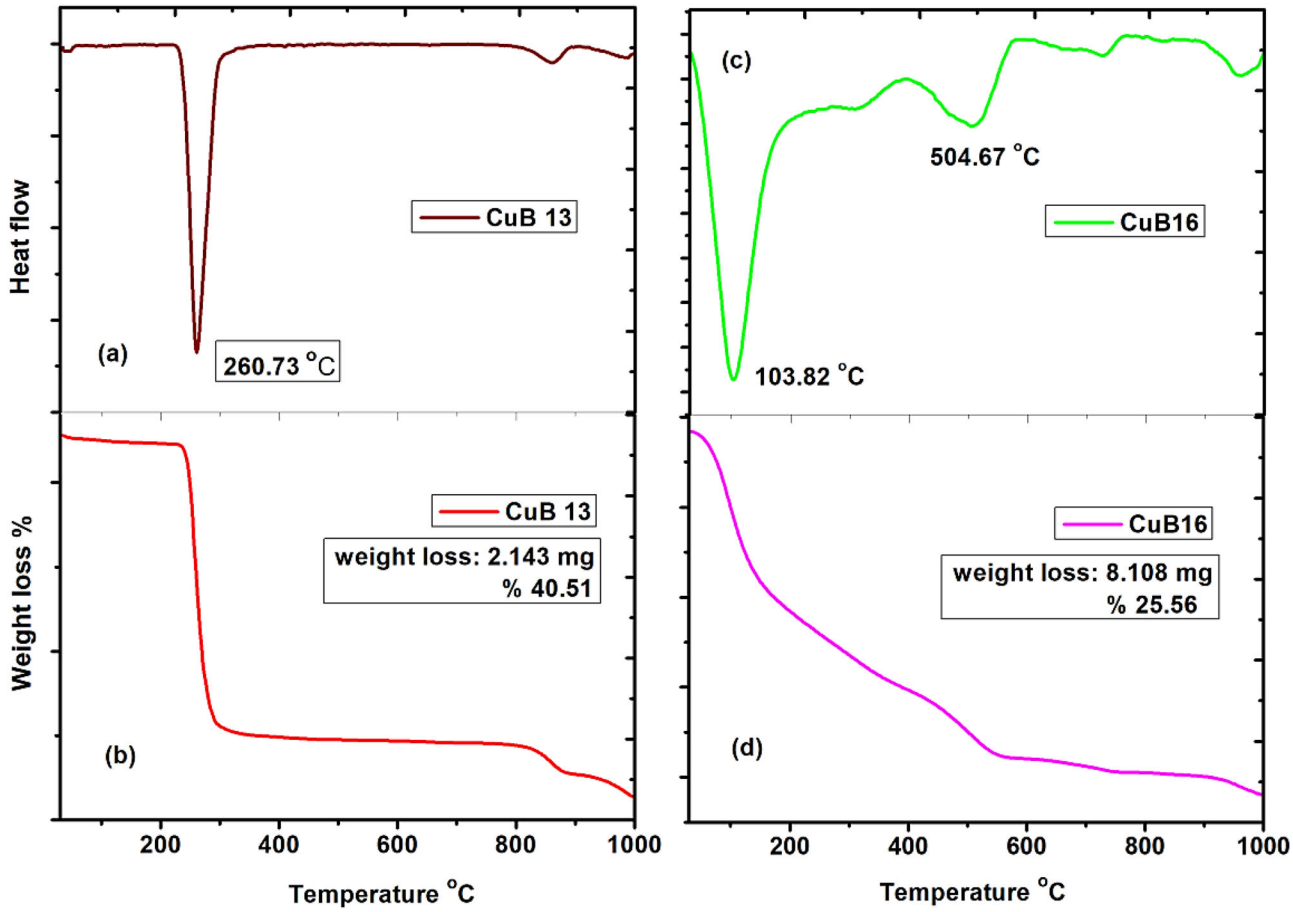

Figure 14. (a) DTA curve of synthesized CuB13 at 90 °C (Cu/B_2O_3 mole ratio 2:1), (b) TGA curve of synthesis CuB13, (c) DTA curve of synthesized CuB16 at 90 °C (Cu/B_2O_3 mole ratio 1:2), (d) TGA curve of synthesis CuB16.

observable. Two satellite peaks were detected for both Cu 2p peaks.[65–69] B 1s core spectra show the main peak positions at 192 eV due to boron-oxygen species in Figure 12g. The component at 190 eV is associated with the B-O state and the last at 191 eV is associated with Cu-O-B. XPS spectra of B1s for CuB13 unveil peaks at 186 eV indicating the presence of boron in the sample.[70] Figure 12h shows the O 1s core-level spectra for CuB13 sample. More detailed analysis of the O 1s spectra shows the symmetry in the O 1s peak is apparent which would be one type of oxygen site in CuB 13 sample. Therefore, O 1s spectrum was detected for investigation of the peak positions and relative abundance of the different oxygen species.[68] It seems a –OH-type and B-O-type oxygen is clearly detectable. Supplementary Table S2 contains all the XPS atomic compositions.

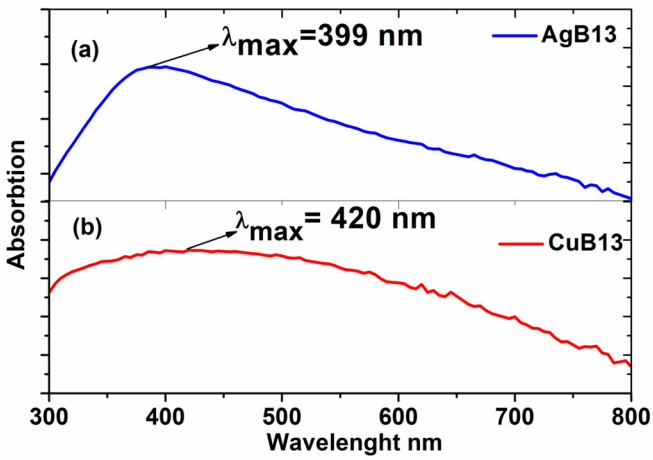

Figure 15. UV-visible spectra of the silver borate and copper borate structure at 90 °C with $Ag(Cu)/B_2O_3$ mole ratio 2:1 – (a) AgB13 and (b) CuB13 nanostructures.

Thermal properties

Figures 13a–d and 14a–d show the TG–DTA graphs of the obtained and selected silver borate and copper borate structures, respectively. From the graphical investigation of the thermal application, the volatile part was determined as the water structure. For this reason, if the extracted water is characterized by the total quantity of starting materials, we can also develop and review the crystal form of the synthesized silver borate and copper borate NPs. In Figure 13a,b, 12.70 wt% amount of weight missing was observed for silver borate NPs (AgB13). This missing occurred at 185.30 °C, 376.30 °C, and 483.80 °C, respectively. When the temperature of sample was increased from 0 to 1000 °C, three molars of the crystal water were determined. Missing of these water can be compared with the calculated rate of 12% and formed $Ag_2O{\cdot}2B_2O_3{\cdot}3H_2O$.

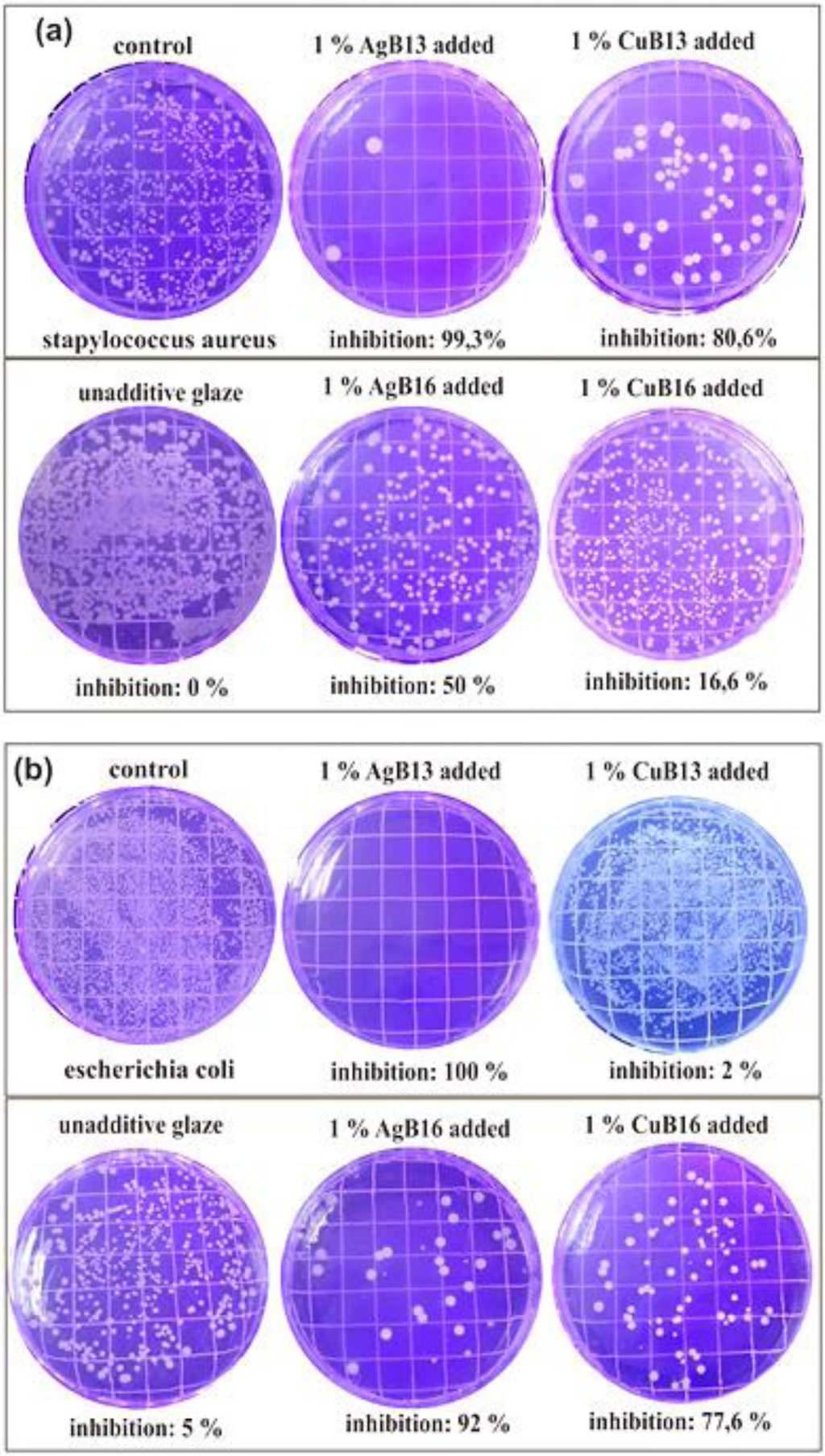

Figure 16. Antibacterial test results of four different borate nanoparticles (1% AgB13, 1% AgB16, 1% CuB13, and 1% CuB16) against (a) *Staphylococcus aureus* and (b) *Escherichia coli*.

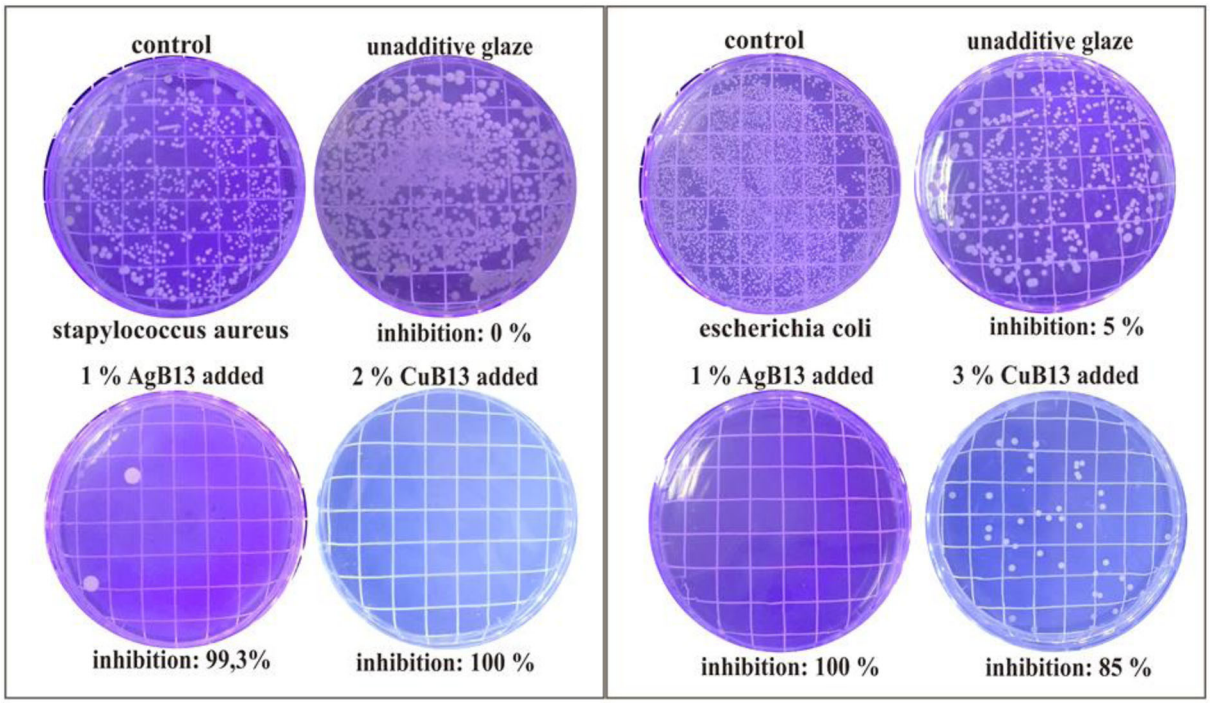

Figure 17. Antibacterial tests of 1% AgB13 and 2% and 3% CuB13 against *Staphylococcus aureus* and *Escherichia coli*.

Table 1. Antibacterial inhibition levels of silver borate and copper borate nanoparticle against *S. aureus* and *E. coli* bacteria.

Product	*S. aureus* (% inhibition)	*E. coli* (% inhibition)
1% AgB13	>99.3	100
1% AgB16	50	92
1% CuB13	80	2
2% CuB13	100	25
3% CuB13	–	85
1% CuB16	16.6	77

Silver borate compound seems losing weight before 190 °C, called the give up of absorbed water and the separation of another evaporating molecule on the surface of $Ag_2O{\cdot}2B_2O_3{\cdot}3H_2O$. The endothermic peak observed which is visible between 185 and 485 °C is the molecular dehydration of the crystallization. Another thermal character was detected for AgB16 particles. In this measurement, 8.4% weight loss is seen till 480 °C (Figure 13c,d). Calculations show that almost one mole of water is less in the formed structure. All the components are lost in one decomposition.

For copper borate NPs (CuB13), totally 40.51 wt% loss was observed which were seen at 260.73 °C. Temperature of the sample was increased from room temperature to 1000 °C, the corresponding missing of a molar crystal water was determined and the $CuO{\cdot}2B_2O_3{\cdot}8H_2O$ structure comparable to the calculated value of 40.51% was determined (Figure 14a,b). For CuB16, thermal investigation shows four different regions and totally 25% weight loss – first 2–3 regions about water removal and the crystal orientation. It seems amount of the water was decreased in this synthesis (Figure 14c,d).

Optical investigation by UV-visible spectra

UV-Vis spectra of silver borate (AgB13) and copper borate (CuB13) compounds were measured between 200 and 800 nm and shown in Figure 15a,b, respectively. These compounds absorb photons at just about 390–420 nm. Therefore, the size of NPs becomes extremely important. In addition, the external faces of the NPs do not give additional information because no major change was observed after 400 nm.

Antibacterial tests

Different percentages of borate NPs (1%, 2%, 3% w/w) were introduced into the industrial ceramic glaze solution containing 14% Al_2O_3, 56% SiO_2, 2%–3% Na_2O, 8% CaO, 5% SO_3. The blend was mixed at 500 rpm for 10 min for a well dispersion. Subsequently, the glazes were applied homogeneously to cover the surfaces by the standard pouring method. The formed wet surfaces were baked for 12 h at 1200 °C.

Produced ceramic glazes (Supplementary Figure S1) were first autoclaved at 121 °C at 1 atm for 20 min. Then it was then placed in 50 mL centrifuge tubes sterilized with 70% ethanol. The bacterial suspension (10^7 CFU mL^{-1}) was dropped to the tubes and incubated at 100 rpm for 24 h in a shaking incubator at 37 °C. At the end of this process, bacterial solutions were diluted. Then, 0.1 mL sample was taken from this suspension and incubated at 37 °C for 24 h. Finally, bacterial colonies were counted and transferred to agar medium. Antibacterial tests of ceramics containing unadditive glaze were also performed. Antibacterial tests were performed by the formula below.[71]

$$\text{Antibacterial performance } (\%) = (\text{A} - \text{B})/\text{A} \times 100$$

where A: control sample; B: the columns taken from the nanomaterial inoculation.

According to the results, 1% AgB13 containing ceramic composition showed the highest antibacterial effect against

S. aureus bacteria when compared to AgB16, CuB13, and CuB 16 (Figure 16a). It seems 1% AgB16, 1% CuB13, and 1% CuB16 does not exactly show the antibacterial effect. Therefore, it is possible to increase the amount of these particles in the ceramic glaze for observing the antibacterial effect. Likewise, against *E. coli* bacteria, 1% AgB13 containing ceramic showed 100% antibacterial effect and when compared to 1% AgB16, 1% CuB13, and 1% CuB16 still it is not possible to observe the full antibacterial effect. Amount of the inhibition changes but desired amount of 99% and more is still discussable (Figure 16b).

If we compare all the results, it is seen that ceramics containing CuB13 does not provide a full protection against *E. coli* bacteria and maybe the effect can be increased with increasing the NP amount. Therefore, in order to increase the antibacterial effect of ceramics containing 2% CuB13 was utilized against *S. aureus* bacteria and 100% protection was detected (Figure 17). Interestingly, the same amount against *E. coli* bacteria showed only 85% inhibition. Hence, it is possible to reveal that CuB13 structure is selectively effective on Gr+ *S. aureus*. More interestingly 3% CuB13, unfortunately, caused the ceramic formation problems during the high temperature application. Consequently, even 1% AgB13 NPs show effective antibacterial features against Gr + and Gr − bacteria, whereas 2% of CuB13 shows selective full antibacterial Gr + effect. However Gr − inhibition efficiency is about 85% and 3% CuB13 is not allowing the formation of a standard ceramic glaze. Table 1 shows the antibacterial inhibition levels of silver borate and copper borate NP against *S. aureus* and *E. coli* bacteria.

Conclusions

In this study, silver and copper borate structures with antibacterial features were obtained and their physical and chemical analysis was performed. During the physical and chemical analysis together with the surface investigation, shape was generally found spherical for AgB structure with around 300 nm size. Also, structure, thermal properties, and morphology of the nanostructures were assigned. Thermal features revealed the percentage of the water molecules inside the particles. XRD patterns and SEM results showed that spherical NPs were produced and no other impurities in the structure. XPS results were also showed the clear formation of the metal borates with clear boron peak positions. Consequently, ceramics having no metal borate glaze showed no antibacterial effect but 1% AgB13 showed perfect antibacterial feature against Gr + and Gr − bacteria. Interestingly, 2% CuB13 showed perfect antibacterial effect against Gr + bacteria but only 85% inhibition against Gr − was observed. As a conclusion, it was shown that metal borate nanostructures were mechanistically investigated and utilized as antibacterial agents in the ceramic industry implying a proper material for the similar applications. Therefore, we can easily conclude that even 1% of borate structure can provide the antibacterial feature in industrial ceramics obtained at 1200 °C.

Authors' contribution

Osman Aguş: Synthesis, analysis and characterization studies, antibacterial studies, interpretation of data – Silver and copper borate nanostructures were mechanistically synthesized.

Osman Arslan: Characterization and analysis studies, antibacterial studies, interpretation of data – Structural analysis, surface properties, crystallinity and all data were investigated and interpreted.

Yüksel Abalı: Planning of the work – Synthesized nanostructures were used for the antibacterial ceramic applications.

Disclosure statement

The authors declare no conflicts of interest.

Funding

We acknowledge the support of the Manisa Celal Bayar University Coordination Unit for Scientific Research Projects (BAP) (Project No: 2014-152) and İstanbul Sabahattin Zaim University, Halal Food Laboratories and IZU-PRO Project (Ag-based Antibacterial Coatings) for basic investigations, and NOS Keskin for antibacterial investigations.

ORCID

Yüksel Abalı https://orcid.org/0000-0002-4165-8656

References

1. Whitman, W. B.; Coleman, D. C.; Wiebe, W. J. Prokaryotes: The Unseen Majority. *Proc. Natl. Acad. Sci. USA* **1998**, *95*, 6578–6583. DOI: 10.1073/pnas.95.12.6578.
2. Donlan, R. M. Biofilms: Microbial Life on Surfaces. *Emerging Infect. Dis.* **2002**, *8*, 881–890. DOI: 10.3201/eid0809.020063.
3. Martelli, G.; Giacomini, D. Antibacterial and Antioxidant Activities for Natural and Synthetic Dual-Active Compounds. *Eur. J. Med. Chem.* **2018**, *158*, 91–105. DOI: 10.1016/j.ejmech.2018.09.009.
4. Ibrahim, N. A.; Eid, B. M.; Abou Elmaaty, T. M.; El-Aziz, E. A. A Smart Approach to Add Antibacterial Functionality to Cellulosic Pigment Prints. *Carbohydr. Polym.* **2013**, *94*, 612–618. DOI: 10.1016/j.carbpol.2013.01.040.
5. Abou Elmaaty, T.; Ramadan, S. M.; Eldin, S. M. N.; Elgamal, G. One Step Thermochromic Pigment Printing and Ag NPs Antibacterial Functional Finishing of Cotton and Cotton/PET Fabrics. *Fibers Polym.* **2018**, *19*, 2317–2323. DOI: 10.1007/s12221-018-8609-x.
6. Yang, H. H.; Liu, Q.; Masse, S.; Zhang, H.; Li, L. F.; Coradin, T. Hierarchically-Organized, Well-Dispersed Hydroxyapatite-Coated Magnetic Carbon with Combined Organics and Inorganics Removal Properties. *Chem. Eng. J.* **2015**, *275*, 152–159. DOI: 10.1016/j.cej.2015.04.026.
7. Wei, A.; Yao, Y.; Wang, T.; Shen, L.; Jia, L.; Chen, S. Decoration of Ag Nanoparticles on the Apatite Nanosheet-Coated Silica Nanofibers with Enhanced Anti-Bacterial Property and Photo-Catalytic Activity. *Mater. Lett.* **2018**, *230*, 236–240. DOI: 10.1016/j.matlet.2018.07.129.
8. Hoseinnejad, M.; Jafari, S. M.; Katouzian, I. Inorganic and Metal Nanoparticles and Their Antimicrobial Activity in Food Packaging Applications. *Crit. Rev. Microbiol.* **2018**, *44*, 161–181. DOI: 10.1080/1040841X.2017.1332001.

9. Hajipour, M. J.; Fromm, K. M.; Ashkarran, A. A.; de Aberasturi, D. J.; de Larramendi, I. R.; Rojo, T.; Serpooshan, V.; Parak, W. J.; Mahmoudi, M. Antibacterial Properties of Nanoparticles. *Trends Biotechnol.* **2012**, *30*, 499–511. DOI: 10.1016/j.tibtech.2012.06.004.
10. Chernousova, S.; Epple, M. Silver as Antibacterial Agent: Ion, Nanoparticle, and Metal. *Angew. Chem. Int. Ed. Engl.* **2013**, *52*, 1636–1653. DOI: 10.1002/anie.201205923.
11. Nasajpour, A.; Ansari, S.; Rinoldi, C.; Rad, A. S.; Aghaloo, T.; Shin, S. R.; Mishra, Y. K.; Adelung, R.; Swieszkowski, W.; Annabi, N.; et al. A Multifunctional Polymeric Periodontal Membrane with Osteogenic and Antibacterial Characteristics. *Adv. Funct. Mater.* **2018**, *28*, 1703437. DOI: 10.1002/adfm.201703437.
12. Aguş, O.; Abalı, Y.; Arslan, O.; San Keskin, N. O. Facile and Controlled Production of Silver Borate Nanoparticles. *SN Appl. Sci.* **2019**, *1*, 662. 2-019-0686-y. DOI: 10.1007/s4245.
13. Zazo, H.; Colino, C. I.; Lanao, J. M. Current Applications of Nanoparticles in Infectious Diseases. *J. Control Release* **2016**, *224*, 86–102. DOI: 10.1016/j.jconrel.2016.01.008.
14. Hao, X.; Chen, S.; Qin, D.; Zhang, M.; Li, W.; Fan, J.; Wang, C.; Dong, M.; Zhang, J.; Cheng, F.; Guo, Z. Antifouling and Antibacterial Behaviors of Capsaicin-Based pH Responsive Smart Coatings in Marine Environments. *Mater. Sci. Eng. C Mater. Biol. Appl.* **2020**, *108*, 110361. DOI: 10.1016/j.msec.2019.110361.
15. Lin, J.; Chen, X. Y.; Chen, C. Y.; Hu, J. T.; Zhou, C. L.; Cai, X. F.; Wang, W.; Zheng, C.; Zhang, P. P.; Cheng, J.; et al. Durably Antibacterial and Bacterially Antiadhesive Cotton Fabrics Coated by Cationic Fluorinated Polymers. *ACS Appl. Mater. Interfaces* **2018**, *10*, 6124–6136. DOI: 10.1021/acsami.7b16235.
16. Luo, X.-L.; Pei, F.; Wang, W.; Qian, H.; Miao, K.-K.; Pan, Z.; Chen, Y.-S.; Feng, G.-D. Microwave Synthesis of Hierarchical Porous Materials with Various Structures by Controllable Desilication and Recrystallization. *Microporous Mesoporous Mater.* **2018**, *262*, 148–153. DOI: 10.1016/j.micromeso.2017.11.037.
17. Shi, C.; Qi, H.; Ma, R.; Sun, Z.; Xiao, L.; Wei, G.; Huang, Z.; Liu, S.; Li, J.; Dong, M.; et al. N,S-Self-Doped Carbon Quantum Dots from Fungus Fibers for Sensing Tetracyclines and for Bioimaging Cancer Cells. *Mater. Sci. Eng. C Mater. Biol. Appl.* **2019**, *105*, 110132. DOI: 10.1016/j.msec.2019.110132.
18. Tuomela, S.; Autio, R.; Buerki-Thurnherr, T.; Arslan, O.; Kunzmann, A.; Andersson-Willman, B.; Wick, P.; Mathur, S.; Scheynius, A.; Krug, H. F.; et al. Gene Expression Profiling of Immune-Competent Human Cells Exposed to Engineered Zinc Oxide or Titanium Dioxide Nanoparticles. *PLoS One.* **2013**, *8*, e68415. DOI: 10.1371/journal.pone.0068415.
19. Arslan, O.; Uyar, T. Multifunctional Electrospun Polymeric Nanofibrous Mats for Catalytic Reduction, Photocatalysis and Sensing. *Nanoscale* **2017**, *9*, 9606–9614. DOI: 10.1039/c7nr02658g.
20. Bonetta, S.; Bonetta, S.; Motta, F.; Strini, A.; Carraro, E. Photocatalytic Bacterial Inactivation by TiO_2-Coated Surfaces. *AMB Express* **2013**, *3*, 59. DOI: 10.1186/2191-0855-3-59.
21. Raghupathi, K. R.; Koodali, R. T.; Manna, A. C. Size-Dependent Bacterial Growth Inhibition and Mechanism of Antibacterial Activity of Zinc Oxide Nanoparticles. *Langmuir* **2011**, *27*, 4020–4028. DOI: 10.1021/la104825u.
22. Ronen, A.; Semiat, R.; Dosoretz, C. G. Antibacterial Efficiency of Composite Nano-ZnO in Biofilm Development in Flow-Through Systems. *Desalin. Water Treat.* **2012**, *3994*, 1–9. DOI: 10.1080/19443994.2012.693698.
23. Tsuang, Y.-H.; Sun, J.-S.; Huang, Y.-C.; Lu, C.-H.; Chang, W. H.-S.; Wang, C.-C. Studies of Photokilling of Bacteria Using Titanium Dioxide Nanoparticles. *Artif. Organs.* **2008**, *32*, 167–174. DOI: 10.1111/j.1525-1594.2007.00530.x.
24. Agarwal, A.; Weis, T. L.; Schurr, M. J.; Faith, N. G.; Czuprynski, C. J.; McAnulty, J. F.; Murphy, C. J.; Abbott, N. L. Surfaces Modified with Nanometer-Thick Silver-Impregnated Polymeric Films That Kill Bacteria but Support Growth of Mammalian Cells. *Biomaterials* **2010**, *31*, 680–690. DOI: 10.1016/j.biomaterials.2009.09.092.
25. Rai, R.; Bai, V. J. *Nanoparticles and Their Potential Application as Antimicrobials*; Department of Studies in Microbiology, University of Mysore: Manasagangotri, Mysore, India, 2011; pp. 197–209.
26. Buerki-Thurnherr, T.; Xiao, L.; Diener, L.; Arslan, O.; Hirsch, C.; Maeder-Althaus, X.; Grieder, K.; Wampfler, B.; Mathur, S.; Wick, P.; Harald, F. K. In Vitro Mechanistic Study towards a Better Understanding of ZnO Nanoparticle Toxicity. *Nanotoxicology* **2013**, *7*, 402–416. DOI: 10.3109/17435390.2012.666575.
27. Nel, A.; Xia, T.; Madler, L.; Li, N. Toxic Potential of Materials at the Nanolevel. *Science* **2006**, *311*, 622–627. DOI: 10.1126/science.1114397.
28. Parham, S.; Wicaksono, D. H. B.; Bagherbaigi, S.; Lee, S. L.; Nur, H. Antimicrobial Treatment of Different Metal Oxide Nanoparticles: A Critical Review. J. Chinese *Chem. Soc.* **2016**, *63*, 385–393. DOI: 10.1002/jccs.201500446.
29. Arslan, O.; Belkoura, L.; Mathur, S. Swift Synthesis, Functionalization and Phase-Transfer Studies of Ultrastable, Visible Light Emitting Oleate@ ZnO Quantum Dots. *J. Mater. Chem. C* **2015**, *3*, 11965–11973. DOI: 10.1039/C5TC03377B.
30. Arslan, O.; Aadesh, S. P.; Belkoura, L.; Mathur, S. Cysteine Modified Zwitterionic ZnO Quantum Dots. *J. Mater. Res.* **2013**, *28*, 1947–1954. DOI: 10.1557/jmr.2013.161.
31. Siripattanakul-Ratpukdi, S.; Ploychankul, C.; Limpiyakorn, T.; Vangnai, A. S.; Rongsayamanont, C.; Khan, E. Mitigation of Nitrification Inhibition by Silver Nanoparticles Using Cell Entrapment Technique. *J. Nanopart. Res.* **2014**, *16, 1-10*. DOI: 10.1007/s11051-013-2218-9.
32. Zhang, T.; Zhao, Y.; Muhetaer, M.; Wang, K. Silver Nanoparticles Cross-Linked Polyimide Aerogels with Improved High Temperature Microstructure Stabilities and High Mechanical Performances. *Microporous Mesoporous Mater.* **2020**, *297*, 110035. DOI: 10.1016/j.micromeso.2020.110.
33. Bar, H.; Bhui, D. K.; Sahoo, G. P.; Sarkar, P.; De, S. P.; Misra, A. Green Synthesis of Silver Nanoparticles Using Latex of *Jatropha curcas*. *Colloids Surf. A. Physicochem. Eng. Aspects* **2009**, *339*, 134–139. DOI: 10.1016/j.colsurfa.2009.02.008.
34. Alswat, A. A.; Bin Ahmad, M.; Hussein, M. Z.; Ibrahim, N. A.; Saleh, T. A. Copper Oxide Nanoparticles-Loaded Zeolite and Its Characteristics and Antibacterial Activities. *J. Mater. Sci. Technol.* **2017**, *33*, 889–896. DOI: 10.1016/j.jmst.2017.03.015.
35. Ahearn, D. G.; May, L. L.; Gabriel, M. M. Adherence of Organisms to Silver-Coated Surfaces. *J. Ind. Microbiol.* **1995**, *15*, 372–376. DOI: 10.1007/BF01569993.
36. Vasilev, K.; Cook, J.; Griesser, H. J. Antibacterial Surfaces for Biomedical Devices. *Exp. Rev. Med. Devices* **2009**, *6*, 553–567. DOI: 10.1586/erd.09.36.
37. Knetsch, M. L. W.; Koole, L. H. New Strategies in the Development of Antimicrobial Coatings: The Example of Increasing Usage of Silver and Silver Nanoparticles. *Polymers* **2011**, *3*, 340–366. DOI: 10.3390/polym3010340.
38. Cloutier, M.; Mantovani, D.; Rosei, F. Antibacterial Coatings: Challenges, Perspectives, and Opportunities. *Trends Biotechnol.* **2015**, *33*, 637–652. DOI: 10.1016/j.tibtech.2015.09.002.
39. Ivanova, E. P.; Crawford, R. J. *Antibacterial Surfaces*; Springer International Publishing: Cham, 2015.
40. Arslan, O.; Arpac, E.; Sayılkan, H. Siliconcarbide Embedded Hybrid Nanocomposites as Abrasion Resistant Coating. *J. Inorg. Organomet. Polym.* **2010**, *20*, 284–292. DOI: 10.1007/s10904-010-9360-y.
41. Rai, M.; Yadav, A.; Gade, A. Silver Nanoparticles as a New Generation of Antimicrobials. *Biotechnol. Adv.* **2009**, *27*, 76–83. DOI: 10.1016/j.biotechadv.2008.09.002.
42. Franke, S.; Grass, G.; Nies, D. H. The Product of the *ybdE* Gene of the *Escherichia coli* Chromosome Is Involved in Detoxification

of Silver Ions. *Microbiology* **2001**, *147*, 965–972. DOI: 10.1099/00221287-147-4-965.
43. Hasan, J.; Crawford, R. J.; Ivanova, E. P. Antibacterial Surfaces: The Quest for a New Generation of Biomaterials. *Trends Biotechnol.* **2013**, *31*, 295–304. DOI: 10.1016/j.tibtech.2013.01.017.
44. Morison, M.; Moffatt, C.; Bridel-Nixon, J.; Bale, S. *A Color Guide to the Nursing Management of Chronic Wounds*, 2nd ed.; Mosby Inc., St. Louis,, 1997.
45. Laga, M.; Meheus, A.; Piot, P. Epidemiology and Control of Gonococcal Ophthalmia Neonatorum. *Bull. World Health Organ.* **1989**, *67*, 471–477.
46. Tokumaru, T.; Shimizu, Y.; Fox, C. J. Antiviral Activities of Silver Sulfadiazine in Ocular Infection. *Res. Commun. Chem. Pathol. Pharmacol.* **1974**, *8*, 151–158.
47. McLean, R.; Hussain, A.; Sayer, M.; Vincent, M.; Hughes, D.; Smith, T. Antibacterial Activity of Multilayer Silver-Copper Surface Films on Catheter Material. *Can. J. Microbiol.* **1993**, *39*, 895–899. DOI: 10.1139/m93-134.
48. Saint, S.; Elmore, J. G.; Sullivan, S. D.; Emerson, S. S.; Koepsell, T. D. The Efficacy of Silver Alloy-Coated Urinary Catheters in Preventing Urinary Tract Infection: A Metaanalysis. *Am. J. Med.* **1998**, *105*, 236–241. DOI: 10.1016/S0002-9343(98)00240-X.
49. Grass, G.; Rensing, C.; Solioz, M. Metallic Copper as an Antimicrobial Surface. *Appl. Environ. Microbiol.* **2011**, *77*, 1541–1547. DOI: 10.1128/AEM.02766-10.
50. Sudha, V. B. P.; Ganesan, S.; Pazhani, G. P.; Ramamurthy, T.; Nair, G. B.; Venkatasubramanian, P. Storing Drinking-Water in Copper Pots Kills Contaminating Diarrhoeagenic Bacteria. *J. Health. Popul. Nutr.* **2012**, *30*, 17–21. DOI: 10.3329/jhpn.v30i1.11271.
51. Saleh, T. A. Nanocomposite of Carbon Nanotubes/Silica Nanoparticles and Their Use for Adsorption of Pb(II): From Surface Properties to Sorption Mechanism. Desalin. *Water Treat.* **2016**, *57*, 10730–10744. DOI: 10.1080/19443994.2015.1036784.
52. Hu, W.; Huang, J.; Zhang, X.; Zhao, S.; Pei, L.; Zhang, C.; Liu, Y.; Wang, Z. A Mechanically Robust and Reversibly Wettable Benzoxazine/Epoxy/Mesoporous TiO_2 Coating for Oil/Water Separation. *Appl. Surf. Sci.* **2020**, *507*, 145168. DOI: 10.1016/j.apsusc.2019.145168.
53. Zheng, Y.; Wang, X.; Wu, G. Chemical Modification of Carbon Fiber with Diethylenetriaminepenta Acetic Acid/Halloysite Nanotube as a Multifunctional Interfacial Reinforcement for Silicone Resin Composites. *Polym. Adv. Technol.* **2020**, *31*, 527–535. DOI: 10.1002/pat.4793.
54. Zheng, Y.; Chen, L.; Wang, X.; Wu, G. Modification of Renewable Cardanol onto Carbon Fiber for the Improved Interfacial Properties of Advanced Polymer Composites. *Polymers* **2019**, *12*, 45. DOI: 10.3390/polym12010045.
55. Arslan, O.; Arpaç, E.; Sayılkan, F.; Sayılkan, H. Hybrid Sol–Gel Coating on Al. *J. Mater. Sci.* **2007**, *42*, 2138–2142. DOI: 10.1007/s10853-006-1297-8.
56. Xie, P.; Li, Y.; Hou, Q.; Sui, K.; Liu, C.; Fu, X.; Zhang, J.; Murugadoss, V.; Fan, J.; Wang, Y.; et al. Tunneling-Induced Negative Permittivity in Ni/MnO Nanocomposites by a Bio-Gel Derived Strategy. *J. Mater. Chem. C* **2020**, *8*, 3029–3039. DOI: 10.1039/C9TC06378A.
57. Kipcak, A. S.; Senberber, F. T.; Yuksel, S. A.; Derun, E. M.; Piskin, S. Synthesis, Characterisation, Electrical and Optical Properties of Copper Borate Compounds. *Mater. Res. Bull.* **2015**, *70*, 442–448. DOI: 10.1016/j.materresbull.2015.05.003.
58. Shvarts, E. M.; Belousova, R. G. Formation of Tricuprotetraborate $3CuO.2B_2O_3.6H_2O$ in Aqueous Solutions. *Russ. J. Appl. Chem.* **2006**, *79*, 672–673. DOI: 10.1134/S107042720604032X.
59. Behm, H. Hexasodium (*Cyclo*-Decahydroxotetracosaoxohexadecaborato) Dicuprate(II) Dodecahydrate, $Na_6[Cu_2\{B_{16}O_{24}(OH)_{10}\}].12H_2O$. *Acta Crystallogr. C Cryst. Struct. Commun.* **1983**, *39*, 20–22. DOI: 10.1107/S0108270183003455.
60. Heller, G.; Pickardt, J. Über ein Ikosaborat-Ion in hydratisierten Kalium- und Natriumkupferpolyboraten/On an Icosaborate Ion in Hydrated Potassium and Sodium Copper Polyborates. *Z. Naturforsch.* **1985**, *40*, 462–466. DOI: 10.1515/znb-1985-0404.
61. Adams, R. M. *Boron, Metallo-Boron Compounds and Boranes*; New York: Wiley, 1964.
62. Dimitriev, Y.; Bachvarova-Nedelcheva, A.; Iordanova, R. Glass Formation Tendency in the System SeO_2-Ag_2O-B_2O_3. *Mater. Res. Bull.* **2008**, *43*, 1905–1910. DOI: 10.1016/j.materresbull.2007.06.054.
63. Ciceo-Lucacel, R.; Ardelean, I. FT-IR and Raman Study of Silver Lead Borate-Based Glasses. *J. Non-Cryst*. Solids **2007**, *353*, 2020–2024. DOI: 10.1016/j.jnoncrysol.2007.01.066.
64. Gao, X.; Guo, Y.; Tian, Y.; Li, S.; Zhou, S.; Wang, Z. Synthesis and Characterization of Polyurethane/Zinc Borate Nanocomposites. *Colloids Surf. A: Physicochem. Eng. Aspects* **2011**, *384*, 2–8. DOI: 10.1016/j.colsurfa.2010.11.037.
65. Selvarajan, S.; Suganthi, A.; Rajarajan, M. A Novel Highly Selective and Sensitive Detection of Serotonin Based on Ag/Polypyrrole/Cu_2O Nanocomposite Modified Glassy Carbon Electrode. *Ultrason. Sonochem*. **2018**, *44*, 319–330. DOI: 10.1016/j.ultsonch.2018.02.038.
66. Singh Surah, S.; Vishwakarma, M.; Kumar, R.; Nain, R.; Sirohi, S.; Kumar, G. Tuning the Electronic Band Alignment Properties of TiO_2 Nanotubes by Boron Doping. *Results Phys.* **2019**, *12*, 1725–1731. DOI: 10.1016/j.rinp.2019.01.081.
67. Wang, S.; Bian, C.; Jia, B.; Wang, Y.; Jing, X. Structure and Thermal Pyrolysis Mechanism of Poly(Resorcinol Borate) with High Char Yield. *Polym. Degrad. Stab*. **2016**, *130*, 328–337. DOI: 10.1016/j.polymdegradstab.2016.06.006.
68. Sung, J.; Shin, M.; Deshmukh, P. R.; Hyun, H. S.; Sohn, Y.; Shin, W. G. Preparation of Ultrathin TiO_2 Coating on Boron Particles by Thermal Chemical Vapor Deposition and Their Oxidation-Resistance Performance. *J. Alloys Compd.* **2018**, *767*, 924–931. DOI: 10.1016/j.jallcom.2018.07.152.
69. Khattak, G. D.; Mekki, A.; Gondal, M. A. Effect of Laser Irradiation on the Structure and Valence States of Copper in Cu-Phosphate Glass by XPS Studies. *Appl. Surf. Sci.* **2010**, *256*, 3630–3635. DOI: 10.1016/j.apsusc.2009.12.167.
70. Zhang, W.; Yang, B.; Chen, J. Effect of Calcination Temperature on Preparation of Boron-Doped TiO_2 by Sol-Gel Method. *Int. J. Photoenergy* **2012**, *2012*, 1–8. DOI: 10.1155/2012/528637.
71. San Keskin, N. O.; Kiliç, N. K.; Dönmez, G.; Tekinay, T. Green Synthesis of Silver Nanoparticles Using Cyanobacteria and Evaluation of Their Photocatalytic and Antimicrobial Activity. *J. Nano Res.* **2016**, *40*, 120–127. DOI: 10.4028/www.scientific.net/JNanoR.40.120.